

Fast entangling gates on fluxoniums via parametric modulation of plasmon interaction

Peng Zhao,^{1,*} Peng Xu,^{2,3} and Zheng-Yuan Xue^{4,5,1,†}

¹*Quantum Science Center of Guangdong-Hong Kong-Macao Greater Bay Area, Shenzhen 518045, China*

²*Institute of Quantum Information and Technology, Nanjing University of Posts and Telecommunications, Nanjing, Jiangsu 210003, China*

³*State Key Laboratory of Quantum Optics Technologies and Devices, Shanxi University, Taiyuan, 030006, China*

⁴*Key Laboratory of Atomic and Subatomic Structure and Quantum Control (Ministry of Education),
Guangdong Basic Research Center of Excellence for Structure and Fundamental Interactions of Matter,
and School of Physics, South China Normal University, Guangzhou 510006, China*

⁵*Guangdong Provincial Key Laboratory of Quantum Engineering and Quantum Materials,
Guangdong-Hong Kong Joint Laboratory of Quantum Matter,
and Frontier Research Institute for Physics, South China Normal University, Guangzhou 510006, China*

(Dated: February 13, 2026)

In superconducting quantum processors, exploring diverse control methods could offer essential versatility and redundancy to mitigate challenges such as frequency crowding, spurious couplings, control crosstalk, and fabrication variability, thus leading to better system-level performance. Here we introduce a control strategy for fast entangling gates in a scalable fluxonium architecture, utilizing parametric modulation of the plasmon interaction. In this architecture, fluxoniums are coupled via a tunable coupler, whose transition frequency is flux-modulated to control the inter-fluxonium plasmon interaction. A bSWAP-type interaction is activated by parametrically driving the coupler at the sum frequency of the plasmon transitions of the two fluxoniums, resulting in the simultaneous excitation or de-excitation of both plasmon modes. This strategy therefore allows the transitions between computational states and non-computational plasmon states, enabling the accumulation of conditional phases on the computational subspace and facilitating the realization of controlled-phase gates. By focusing on a specific case of these bSWAP-type interactions, we show that a simple drive pulse enables sub-100ns CZ gates with an error below 10^{-4} . Given its operational flexibility and extensibility, this approach could potentially offer a foundational framework for developing scalable fluxonium-based quantum processors.

I. INTRODUCTION

Unlike the well-studied transmon qubit [1], the fluxonium qubit [2] exhibits a complex, strongly anharmonic energy structure. Besides the qubit transition, which typically occurs at frequencies around 100 MHz, the fluxonium also exhibits multiple accessible plasmon transitions spanning a broad range from a few gigahertz to over 10 GHz. On one hand, these plasmon modes in fluxonium systems increase susceptibility to unintended activations of these transitions and spurious inter-mode couplings among fluxonium qubits and ancillary circuits such as readout resonators and couplers, during quantum operations. On the other hand, this spectral richness could provide the essential opportunity to mitigate challenges including frequency crowding [3–5], spurious couplings [4–7], control crosstalk [8], and fabrication variability [9–11], which is particularly critical in large-scale superconducting quantum processors. In this context, these transitions can, and indeed should, be carefully allocated to support distinct quantum operations such as two-qubit gates [12–20], readout [21–26], and initialization [26–29], thereby advancing the development of scalable high-performance fluxonium-based quantum processors. Generally, without detailed consideration of specific qubit characteristics, a potential allocation strategy may seek to maximize frequency separation between bands dedicated to distinct operations.

For fluxonium qubits (the lowest five states labeled by $\{|0\rangle, |1\rangle, |2\rangle, |3\rangle, |4\rangle\}$), which are typically biased at the half-flux-quantum sweet spot to achieve high coherence times [30–32], the small electric dipole moment of the qubit transition $|0\rangle \rightarrow |1\rangle$ complicates its use in quantum operations beyond single-qubit gates [33, 34], particularly within large-scale systems. However, among accessible higher-energy transitions, three plasmon transitions, namely $|0\rangle \rightarrow |3\rangle$, $|1\rangle \rightarrow |2\rangle$, and $|1\rangle \rightarrow |4\rangle$, possess transmon-like dipole moments, making them particularly relevant for implementing various quantum operations. Specifically, these transitions can facilitate strong dispersive coupling with readout resonators, enabling fast, high-fidelity qubit readout [24, 25]. They can also, in principle, be leveraged to realize microwave-activated controlled-phase gates by facilitating transitions between computational states and non-computational states (involving the excitation of these plasmon modes [12] or coupler modes [15]). Apparently, both types of operations could inevitably cause leakage out of the computational subspace, presenting a significant challenge for quantum error correction [36]. Addressing this issue requires the incorporation of leakage removal operations, typically involving engineered interactions between fluxonium plasmons and a dissipative environment such as the readout resonator [29]. It is therefore evident that the practical utilization of plasmon modes in large-scale fluxonium-based quantum processors necessitates a flexible and scalable control strategy for engineering plasmon interactions [19, 37].

Here we introduce a control strategy that employs parametric modulation of the plasmon interaction to implement fast entangling gates on fluxonium qubits, alternative to the commonly used microwave-based approaches with static plasmon-plasmon couplings [12–20]. Within the flux-

*Electronic address: shangniguo@sina.com

†Electronic address: zyxue83@163.com

onium qubit architecture supporting tunable plasmon interactions [19], fluxoniums are coupled via a tunable coupler, see Fig. 1(a). The two-qubit gate can be implemented by applying parametric driving to the coupler at the sum frequency of the selective plasmon modes of the two fluxoniums (e.g., $|1\rangle \rightarrow |2\rangle$ for each fluxonium). This drive activates a bSWAP-type interaction [38–44] (e.g., $|11\rangle \leftrightarrow |22\rangle$) between the selective plasmon modes, enabling the transition between computational states (e.g., $|11\rangle$) and the non-computational states (e.g., $|22\rangle$), see Fig. 1(b). Similar to the microwave-based approaches [12, 15], this transition enables the accumulation of a non-trivial conditional phase on the computational state (e.g., $|11\rangle$) and thus facilitates the implementation of controlled-phase gates. We note that, similar to the schemes studied in Refs. [33–35], employing parametric modulation on the fluxonium qubits could serve as an alternative approach for activating such bSWAP-type transitions.

Considering its features, this strategy offers several potential advantages over traditional microwave-based methods, particularly in large-scale systems: (i) Driving the coupler directly, rather than the qubits, can significantly reduce control crosstalk among nearest-neighbor qubits, an essential feature for densely coupled qubit systems. (ii) The parametric drive frequency can be placed far from frequency bands used for other operations, minimizing unwanted transitions and alleviating spectral crowding. (iii) Parametric-activated gates generally pose less stringent requirements on system parameters (e.g., transition frequencies) [40, 45], offering greater resilience to fabrication variations and parameter misalignments.

Despite these advantages, the proposed strategy shares a significant challenge with conventional microwave-based methods, i.e., the short coherence times of plasmon modes (or coupler modes). Furthermore, since our approach involves doubly excited plasmon states, this coherence limitation is expected to be more severe compared to conventional schemes, which typically utilize only singly excited plasmon states. However, unlike parametric gates in transmon systems, which often exceed 100 ns in gate lengths (see, e.g., Refs. [45–48]; a notable exception is the fast parametric scheme in Ref. [49] with gate times below 25 ns), the present strategy enables sub-100ns CZ gates on fluxoniums with intrinsic errors below 10^{-4} . We therefore expect that, even with coherence times on the order of $\sim 10 \mu\text{s}$, which aligns with typical values in current devices [13, 16], a gate error approaching 10^{-3} remains achievable. Moreover, since the decoherence mechanisms of plasmon modes are similar to those of transmon qubits [13, 30], one can anticipate no fundamental barrier to achieving coherence times approaching $100 \mu\text{s}$ in future implementations. Such an improvement could push gate errors toward the 10^{-4} level. Given all these considerations, we expect this approach may constitute a promising control strategy for the development of large-scale, high-performance fluxonium-based quantum processors.

This paper is organized as follows. In Sec. II, we introduce the model for the fluxonium system with tunable plasmon interactions and derive the effective Hamiltonian of the full system under the parametric modulation. In Sec. III, we ex-

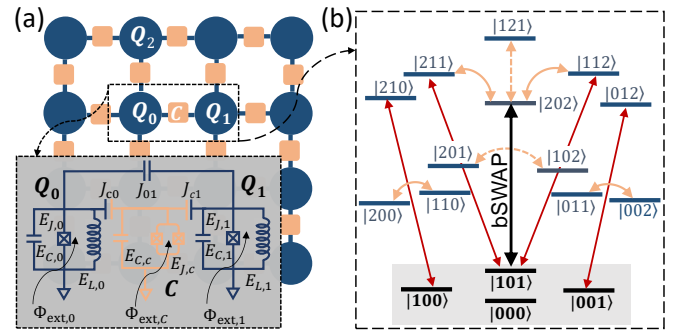


FIG. 1: (a) A two-dimensional (2D) square qubit lattice comprising fluxoniums (circles) coupled via couplers (squares). The inset depicts the fluxonium architecture featuring tunable plasmon interactions, where fluxoniums are coupled via a frequency-tunable transmon coupler. (b) The energy levels of the unit cell comprising two coupled fluxonium qubits (i.e., Q_0 and Q_1), with emphasis on the computational subspace spanned by $\{|000\rangle, |001\rangle, |100\rangle, |101\rangle\}$ (shaded region) and the fluxonium's plasmon mode $|1\rangle \rightarrow |2\rangle$. The full system state is labeled as $|Q_0, C, Q_1\rangle$. Solid orange arrows indicate direct plasmon-coupler couplings, while dashed orange arrows represent coupler-mediated plasmon-plasmon interactions. In addition to blue sideband transitions between each fluxonium and the coupler (red arrows), parametric modulation of the coupler can also activate a bSWAP-type interaction ($|101\rangle \rightarrow |202\rangle$, black arrow) between the plasmon modes of the two fluxoniums.

amine various parametric-activated bSWAP-type interactions within the fluxonium system, with a focus on one specific case: the $|11\rangle \leftrightarrow |22\rangle$ transition. In Sec. IV, we detail our control strategy for implementing fast, high-fidelity two-qubit controlled-phase (CZ) gates based on the parametric-activated $|11\rangle \leftrightarrow |22\rangle$ transition. In Sec. V, we summarize our main results and discuss potential directions for future work.

II. THE FLUXONIUM SYSTEM WITH PARAMETRIC MODULATION

The fluxonium coupling architecture considered in this work is schematically depicted in Fig. 1(a). Within this architecture, the unit cell comprising two coupled fluxonium qubits is modeled by the Hamiltonian (with $\hbar = 1$ hereafter)

$$\begin{aligned} \hat{H} = & \sum_{k=0,1} [4E_{C,k}\hat{n}_k^2 + \frac{E_{L,k}}{2}(\hat{\varphi}_k - \varphi_{\text{ext},k})^2 - E_{J,k} \cos \hat{\varphi}_k] \\ & + J_{c0}\hat{n}_0\hat{n}_c + J_{c1}\hat{n}_1\hat{n}_c + J_{01}\hat{n}_0\hat{n}_1 \\ & + 4E_{C,c}\hat{n}_c^2 - E_{J,c} \cos(\frac{\varphi_{\text{ext},c}}{2}) \cos \hat{\varphi}_c, \end{aligned} \quad (1)$$

where the first and last lines describe the two fluxonium qubits ($k = 0, 1$) and the frequency-tunable transmon coupler (c), respectively, while the second line accounts for both the fluxonium-coupler couplings and the direct fluxonium-fluxonium coupling. Here, E_C , E_J , and E_L denote the charging, Josephson, and inductive energies, respectively, and φ_{ext} represents the external phase bias, defined as $\varphi_{\text{ext}} =$

$2\pi\Phi_{\text{ext}}/\Phi_0$ (Φ_0 is the flux quantum). Throughout this work, both fluxonium qubits are biased at their half-flux-quantum sweet spots with $\varphi_{\text{ext},k} = \pi$, unless stated otherwise.

Owing to the small electric transition dipole moment of the computational (qubit) transition, which effectively decouples the qubit states from the coupler, we focus on coupler-mediated plasmon-plasmon interactions. Following Ref. [19], we approximate the transmon coupler as an anharmonic oscillator and restrict our attention to one specific plasmon mode per fluxonium (e.g., $|j\rangle \rightarrow |l\rangle$ in Q_0 and $|r\rangle \rightarrow |t\rangle$ in Q_1). Under these approximations, the system Hamiltonian in Eq. (1) can be reduced to the form (see Appendix A for details):

$$\hat{H}_p = \sum_{k=0,1} \left[\omega_{p,k} \hat{p}_k^\dagger \hat{p}_k + g_{p,ck} (\hat{p}_k + \hat{p}_k^\dagger) (\hat{a}_c + \hat{a}_c^\dagger) \right] + \omega_c \hat{a}_c^\dagger \hat{a}_c + \frac{\alpha_c}{2} \hat{a}_c^\dagger \hat{a}_c^\dagger \hat{a}_c \hat{a}_c + g_{p,01} (\hat{p}_0 + \hat{p}_0^\dagger) (\hat{p}_1 + \hat{p}_1^\dagger), \quad (2)$$

where

$$\begin{aligned} \hat{p}_0 &= |j\rangle \langle l|, \hat{p}_0^\dagger = |l\rangle \langle j|, \\ \hat{p}_1 &= |r\rangle \langle t|, \hat{p}_1^\dagger = |t\rangle \langle r|, \end{aligned} \quad (3)$$

are the lowering and raising operators for the plasmon modes of the two fluxoniums, with transition frequencies $\omega_{p,0}$ and $\omega_{p,1}$, respectively, a_c (a_c^\dagger) denotes the destroy (creation) operator for the coupler, which has transition frequency ω_c and anharmonicity α_c , and $g_{p,ck}$ and $g_{p,01}$ represent the coupling strengths of the plasmon-coupler couplings and the direct plasmon-plasmon coupling, respectively.

By considering the system to be in the dispersive regime, where the coupler-plasmon detuning $|\Delta_{p,k}| = |\omega_{p,k} - \omega_c|$ is much larger than the coupling strength $g_{p,ck}$, an effective Hamiltonian can be derived by eliminating the plasmon-coupler coupling terms in Eq. (2) using a Schrieffer-Wolff transformation (SWT) [50] (see Appendix A for details). Assuming the coupler remains in its ground state, we focus exclusively on the inter-fluxonium interactions, leading to the following approximate effective Hamiltonian:

$$\hat{H}_{p,\text{eff}} = \sum_{k=0,1} \left[\omega_{p,k} \hat{p}_k^\dagger \hat{p}_k \right] + g_p (\hat{p}_0 + \hat{p}_0^\dagger) (\hat{p}_1 + \hat{p}_1^\dagger). \quad (4)$$

Here, g_p denotes the strength of the effective plasmon-plasmon interaction, given by

$$g_p = g_{p,01} + \frac{g_{p,0}g_{p,1}}{2} \left[\sum_{k=0,1} \left(\frac{1}{\Delta_{p,k}} - \frac{1}{S_{p,k}} \right) \right]. \quad (5)$$

with $S_{p,k} = \omega_{p,k} + \omega_c$. Note that for clarity, the frequency renormalization of the plasmon transitions resulting from plasmon-coupler interactions has been omitted.

Given the tunability of the plasmon interaction through coupler frequency adjustments, as expressed in Eq. (5), we now introduce a single-tone parametric drive of the form

$$\Phi_{\text{ext},c}(t) = \Phi_s + \delta_\Phi \cos(\omega_p t + \phi_0) \quad (6)$$

applied to the coupler to rapidly modulate its frequency [40, 45]. Here, Φ_s denotes the static coupler bias, while δ_Φ , ω_p , and ϕ_0 are the amplitude, the frequency, and the initial phase of the drive, respectively. For simplicity, we assume $\phi_0 = 0$ hereafter. Under the small-modulation condition ($\delta_\Phi \ll 1$), the coupler frequency under such rapid modulation can be approximated to first order in δ_Φ as:

$$\omega_c(\Phi_{\text{ext},c}) \approx \omega_c(\Phi_s) + \frac{\partial \omega_c}{\partial \Phi_{\text{ext},c}} \Big|_{\Phi_s} \delta_\Phi \cos(\omega_p t). \quad (7)$$

By substituting the expression for g_p from Eq. (5) with the expanded form of $\omega_c(\Phi_{\text{ext},c})$ and further expanding g_p to first order in $\delta_\Phi \cos(\omega_p t)$ [40, 45], we can derive an effective Hamiltonian in a rotating frame defined by the plasmon mode frequencies. Under the assumptions that $\omega_{p,0} > \omega_{p,1}$ and that fast-oscillating terms can be neglected, the effective Hamiltonian takes the form:

$$\hat{H}_{p,\text{eff}} \approx g_{\text{eff}} e^{+i\omega_p t} \left(e^{-i\Delta_{p,01} t} \hat{p}_0 \hat{p}_1^\dagger + e^{-i\Delta_{p,01} t} \hat{p}_0^\dagger \hat{p}_1 \right) + h.c. \quad (8)$$

with

$$\begin{aligned} g_{\text{eff}} &= \delta_\Phi \frac{\partial g_p}{\partial \Phi_{\text{ext},c}} \Big|_{\Phi_s} \\ &= \delta_\Phi \frac{g_{p,0}g_{p,1}}{4} \frac{\partial \omega_c}{\partial \Phi_{\text{ext},c}} \Big|_{\Phi_s} \left[\sum_{k=0,1} \left(\frac{1}{\Delta_{p,k}^2} + \frac{1}{S_{p,k}^2} \right) \right], \end{aligned} \quad (9)$$

$\Delta_{p,01} = \omega_{p,0} - \omega_{p,1}$, and $S_{p,01} = \omega_{p,0} + \omega_{p,1}$. The first and second terms in parentheses in Eq. (8) describe SWAP-type and bSWAP-type interactions between the plasmon modes of the two fluxoniums, respectively. It should be noted that, as indicated in Eq. (4), although the coupled fluxonium system inherently exhibits both static SWAP-type and bSWAP-type plasmon interactions, the plasmon modes of the two fluxoniums are typically far detuned. This detuning renders the contribution from these static interactions non-dominant under the rotating-wave approximation.

Since the SWAP-type plasmon interaction involves only non-computational states and the present work focuses on realizing two-qubit gates, we concentrate on the bSWAP-type plasmon interactions (blue sideband transitions), which enable transitions between computational and non-computational plasmon states. As indicated by Eq. (8), such interactions are activated when the parametric drive frequency satisfies $\omega_p = \omega_{p,0} + \omega_{p,1}$, i.e., matches the sum frequency of the two fluxoniums' plasmon transitions.

Note that while the approximate model derived above offers useful physical insight into parametric-activated plasmon interactions, it omits several important features. As shown in Fig. 1(b), in addition to the bSWAP-type interaction, sideband transitions between each fluxonium and the coupler are also present [51]. Furthermore, unlike the expression in Eq. (5) derived under the adiabatic approximation, the coupling strengths for SWAP-type and bSWAP-type interactions are generally distinct [40]. A more rigorous treatment using time-dependent Schrieffer-Wolff transformation can be found in Refs. [40, 52]; however, the resulting expressions do not

yield significant additional insight beyond the current model. Therefore, we retain the approximate model in the following analysis.

III. PARAMETRIC-ACTIVATED BSWAP-TYPE PLASMON INTERACTION

TABLE I: The circuit Hamiltonian parameters of the coupled fluxonium system shown in the inset of Fig. 1. The values in parentheses correspond to the configuration with reduced fluxonium-coupler coupling strength and Josephson energy of the transmon coupler.

(GHz)	$E_C/2\pi$	$E_L/2\pi$	$E_J/2\pi$
Fluxonium Q_0	1.41	0.80	6.27
Fluxonium Q_1	1.30	0.59	5.71
Transmon C	0.32	—	55 (40)
Spectator Q_2	1.33	0.60	5.40
(MHz)	$J_{c0}/2\pi$	$J_{c1}/2\pi$	$J_{01}/2\pi$
Coupling strengths	500 (300)	500 (300)	125 (80)

TABLE II: The fluxonium frequencies and the maximum coupler frequencies of the coupled fluxonium system with the circuit Hamiltonian parameters listed in Table I.

(GHz)	$\omega_{01}/2\pi$	$\omega_{12}/2\pi$	$\omega_{03}/2\pi$	$\omega_{14}/2\pi$
Q_0	0.298	5.621	8.347	12.293
Q_1	0.222	5.269	7.461	11.019
C	11.537 (9.788)	11.194 (9.441)	-	-

In this section, we present a numerical analysis of bSWAP-type plasmon interactions in the coupled fluxonium system, based on the approximate model and using the circuit parameters summarized in Table I (primarily drawn from Ref. [16]). For convenience, the corresponding fluxonium and coupler frequencies are provided in Table II. Prior to detailing the system's behavior under parametric driving, we first examine the tunable plasmon interactions within the architecture. Hereafter, the system state is denoted as $|Q_1, C, Q_2\rangle$ and when referring exclusively to the fluxonium subspace, the notation $|Q_1, Q_2\rangle \equiv |Q_1, 0, Q_2\rangle$ is used.

A. Tunable plasmon interaction

For illustration purposes only, here we focus on the coupled-mediated interaction for the plasmon transition $|1\rangle \rightarrow |2\rangle$. As demonstrated in previous studies [12, 19], the inter-fluxonium plasmon interaction can induce conditional frequency shifts in the plasmon transition. Accordingly, to quantify the interaction strength, we adopt the metric of state-dependent frequency shifts [19], defined as

$$\begin{aligned} \delta\omega_{p,0} &= |(E_{21} - E_{11}) - (E_{20} - E_{10})|, \\ \delta\omega_{p,1} &= |(E_{12} - E_{11}) - (E_{02} - E_{01})|, \end{aligned} \quad (10)$$

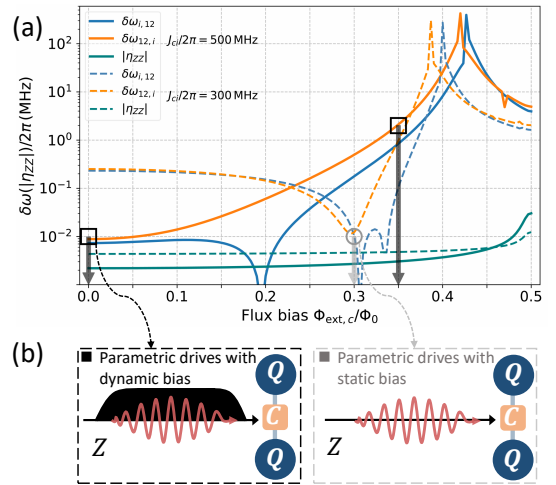


FIG. 2: (a) Coupler-mediated interactions for the plasmon transition $|1\rangle \rightarrow |2\rangle$, characterized by state-dependent plasmon frequency shifts as a function of coupler flux bias. Discontinuities and abrupt jumps in the curves result from state labeling ambiguities near avoided crossings. Solid and dashed lines represent results for coupled fluxonium systems with distinct parameter sets, including coupling strengths and coupler frequencies, as specified in Table I. Black arrows indicate the coupler idle point (where state-dependent frequency shifts are minimized) and interaction point for the system with $J_{ck}/2\pi = 500$ MHz, while gray arrows mark the corresponding points for the system with $J_{ck}/2\pi = 300$ MHz. (b) In the context of implementing parametric gates, these parameter sets lead to two distinct operational configurations: the left panel illustrates the combination of a parametric drive with a dynamic flux bias, while the right panel shows the combination of a parametric drive with a static flux bias.

for the two fluxoniums, respectively, where E_{kl} denotes the energy of the system eigenstate $|kl\rangle$. Using the circuit parameters in Table I, Figure 2(a) shows the plasmon interaction-induced shift as a function of coupler flux bias for two distinct parameter sets. The corresponding ZZ coupling strength is also shown, confirming that the computational states are effectively decoupled.

As indicated by Eq. (9), the strength of the parametric-activated interaction is proportional to the derivative of the plasmon interaction with respect to the coupler flux bias, i.e., $\partial g_p / \partial \Phi_{\text{ext},c}$. Thus, as shown in Figs. 2(a) and 2(b), two operational configurations can be identified for implementing parametric gates. When the derivative at the system (coupler) idle point, where state-dependent frequency shifts are minimized, is insufficient to achieve strong parametric-activated interaction, a dynamic bias is required to shift the coupler from its idle point to an interaction point that provides a larger derivative, as exemplified by systems with $J_{ck}/2\pi = 500$ MHz. Conversely, when the derivative at the idle point already supports strong parametric-activated interaction, only a static bias is needed, which is the case for systems with $J_{ck}/2\pi = 300$ MHz.

Note that from a control complexity perspective, the static-bias configuration is often preferable [47]. However, success-

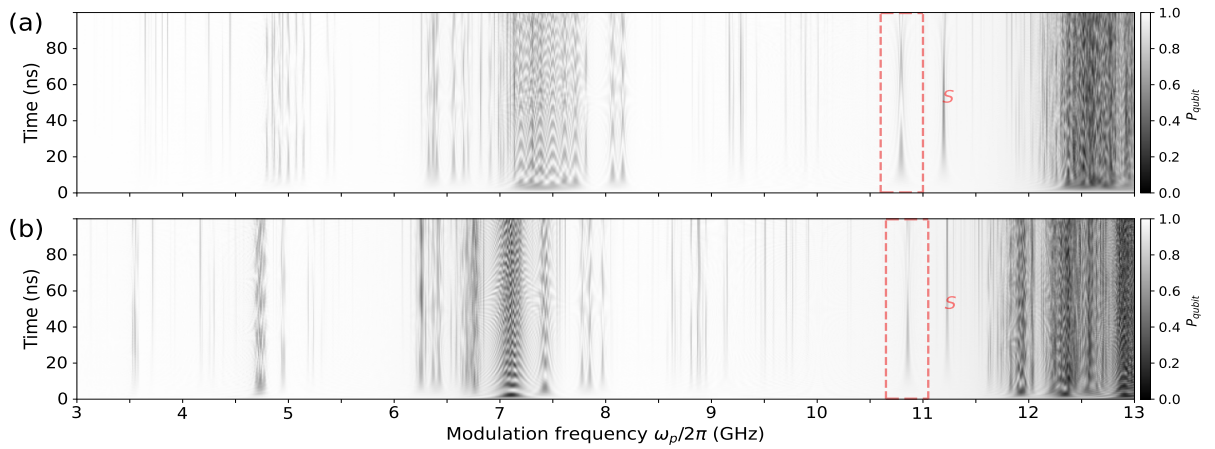


FIG. 3: Population within the computational (qubit) subspace as a function of parametric drive frequency and evolution time, for the coupled fluxonium system initialized in the state $(|00\rangle + |01\rangle + |10\rangle + |11\rangle)/2$. (a) System with $J_{ck}/2\pi = 500$ MHz. The static coupler bias is set to $\Phi_s/\Phi_0 = 0.35$, and the parametric drive amplitude is $\delta_\Phi/\Phi_0 = 0.045$. (b) System with $J_{ck}/2\pi = 300$ MHz. The static coupler bias is set to $\Phi_s/\Phi_0 = 0.30$, and the drive amplitude is $\delta_\Phi/\Phi_0 = 0.075$. The pink dashed boxes highlight the parametric-activated transition $|11\rangle \rightarrow |22\rangle$, while the pink label S indicates an example of a spurious transition induced by the parametric drive, specifically $|000(100)\rangle \leftrightarrow |004(104)\rangle$.

ful implementation of parametric gates under this approach may impose stricter constraints on circuit parameters. In contrast, the dynamic flux-bias configuration can offer greater flexibility in selecting bias parameters [46] and provide operational redundancy to mitigate challenges such as spurious couplings to defect modes [6, 53–56].

B. Parametric-activated interaction

Here we turn to analyze parametric-activated interactions in the coupled fluxonium system, with particular emphasis on the bSWAP-type interaction of $|11\rangle \leftrightarrow |22\rangle$. Before examining this specific interaction in detail, we provide a broader overview of the parametric processes activated by rapid flux modulation of the coupler frequency. This overview could offer insight beyond the approximate model introduced in Sec. II and helps illustrate both potential challenges and opportunities for implementing fast, high-fidelity entangling gates in this architecture.

Under the parametric drive described by Eq. (6), Figure 3 displays the population within the computational subspace as a function of modulation frequency and evolution time for the coupled fluxonium system initialized in the state $(|00\rangle + |01\rangle + |10\rangle + |11\rangle)/2$. In Fig. 3(a), with a static coupler bias of $\Phi_s/\Phi_0 = 0.35$, a modulation amplitude of $\delta_\Phi/\Phi_0 = 0.045$, and a coupling strength of $J_{ck}/2\pi = 500$ MHz, numerous chevron patterns are observed across the frequency range from 3 GHz to 13 GHz. Each pattern generally corresponds to a specific parametric-activated transition. Similar behavior is evident in Fig. 3(b) for the system with $J_{ck}/2\pi = 300$ MHz, where the static coupler bias and drive amplitude are $\Phi_s/\Phi_0 = 0.30$ and $\delta_\Phi/\Phi_0 = 0.075$, respectively.

As previously noted, the intrinsic nonlinearity of the transmon coupler enables rapid flux modulation of its frequency to activate both bSWAP-type transitions between coupled plasmon modes and various other transitions, such as blue sideband transitions between fluxonium plasmon modes and the coupler (see Appendix B 1 for details). Based on their physical origins, these transitions can be classified into three main categories:

(1) bSWAP-type transitions for plasmon mode pairs, including transitions within the same plasmon mode of the two fluxoniums (e.g., $|11\rangle \rightarrow |22\rangle$, highlighted by the pink dashed boxes, and $|00\rangle \rightarrow |33\rangle$) and between different modes (e.g., $|01\rangle \rightarrow |34\rangle$ and $|10\rangle \rightarrow |23\rangle$), as suggested by the discussion given in Sec. II;

(2) Blue sideband transitions between the fluxonium plasmon modes and the coupler, such as $|001\rangle \rightarrow |014\rangle$ and $|001\rangle \rightarrow |311\rangle$;

(3) Coupler state excitations due to effective two-photon (squeezing) drives, for example $|000\rangle \rightarrow |020\rangle$, which arise from the flux modulation of the coupler’s nonlinear potential [35], see Appendix B 2 for details.

In addition to these main categories, strong state hybridization among fluxonium plasmon modes and the coupler, resulting from their strong couplings, can induce parametric-activated cross-driving transitions (facilitated by the three main types of transitions described above). These are analogous to cross-resonance effects in microwave-driven coupled qubit systems [57–60] and can give rise to various high-energy transitions through single- or multi-photon processes when on-resonance conditions (frequency collisions) are inadvertently met [61–64]. A typical example is the transition $|000\rangle \rightarrow |004\rangle$ (labeled S , see Fig. 3), which is prohibited for the bare fluxonium at the half flux quantum sweet spot but becomes allowed in the coupled system due to hybridization

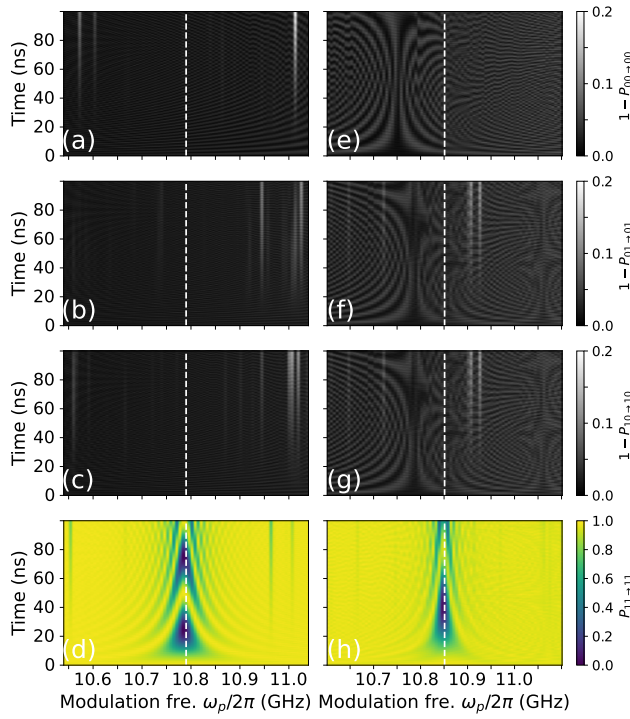


FIG. 4: Population versus the parametric drive frequency around the $|11\rangle \rightarrow |22\rangle$ transition and the evolution time, presented as an enlarged view of the region within the pink dashed box in Fig. 3. Here, $P_{ij \rightarrow ij}$ represents the population in state $|ij\rangle$ when the system is initially prepared in $|ij\rangle$. The circuit parameters used in (a-d) and (e-h) are the same as those in Fig. 3(a) and Fig. 3(b), respectively. The vertical dashed lines indicate the ideal transition frequency for $|11\rangle \rightarrow |22\rangle$ without accounting for drive-induced frequency shifts.

between between $|004\rangle$ and $|013\rangle$.

TABLE III: Transition parameters at the interaction point for the coupled fluxonium system with the circuit Hamiltonian parameters listed in Table I.

	$ 0\langle \hat{n}_k 1\rangle $	$ 1\langle \hat{n}_k 2\rangle $	$ 0\langle \hat{n}_k 3\rangle $	$ 1\langle \hat{n}_k 4\rangle $
Q_0	0.068	0.562	0.488	0.214
Q_1	0.057	0.557	0.498	0.202
$C(\Phi_s)$	$\omega_{01}/2\pi$	$\omega_{12}/2\pi$	$ 0\langle \hat{n}_c 1\rangle $	$ 1\langle \hat{n}_c 2\rangle $
0.35	7.661	7.305	1.223	1.689
0.30	7.423	7.066	1.204	1.661

In general, aside from the targeted transitions such as $|11\rangle \rightarrow |22\rangle$ (see Fig. 4 for an enlarged view of the area within the dashed pink box in Fig. 3) studied here for realizing two-qubit gates, all other transitions, particularly those spectrally close to the target transition, can complicate gate control and degrade performance. Furthermore, when seeking higher gate speeds through stronger parametric drives or coupling strengths, higher-order spurious transitions, though typically faint here (see Figs. 3 and 4), may become non-negligible. These unwanted transitions introduce frequency collision is-

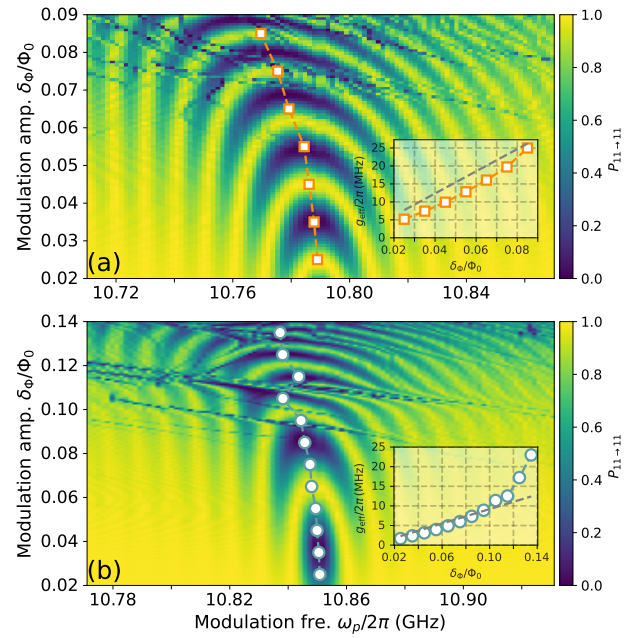


FIG. 5: Population in $|11\rangle$ in the parametric-driven system as a function of the parametric drive frequency around the $|11\rangle \rightarrow |22\rangle$ transition and the drive amplitude, with the evolution time fixed at 100 ns and the initial state of $|11\rangle$. The circuit parameters used in (a) and (b) correspond to those in Fig. 3(a) and Fig. 3(b), respectively. The orange square in (a) and the teal circle in (b) mark the transition frequencies of $|11\rangle \rightarrow |22\rangle$ obtained using the Floquet numerical method. The corresponding transition strengths are shown in the insets, with grey lines indicating the results from the approximate model.

sues that intensify with increasing drive magnitudes and coupling strengths.

However, unlike transmon-based systems [65], the fluxonium qubit benefits from its strong anharmonicity, small qubit transition dipole moment, and transmon-like plasmon transition dipoles. This enables the implementation of strong parametric-activated interactions without significant interference from other spurious transitions, even when the coupled plasmon-coupler system operates in the non-dispersive regime [66–68] (see the coupling parameters listed in Table III) and under large modulation amplitudes. Specifically, as shown in Figs. 3 and 4, the target $|11\rangle \rightarrow |22\rangle$ transition remains well separated from other significant spurious transitions and there does not exhibit notable frequency crowding issues, even at activated strengths exceeding 5 MHz (corresponding to oscillation periods below 100 ns).

To explore the limits of such collision-free behavior, Figure 5 shows the population in $|11\rangle$ under flux modulation in the coupled system, which is initially prepared in $|11\rangle$. The population is plotted as a function of both the parametric drive frequency around the $|11\rangle \rightarrow |22\rangle$ transition and the drive amplitude, with the evolution time fixed at 100 ns. In addition, we also employ the Floquet numerical method [52], specifically by numerically computing the quasienergy spec-

trum of the periodically driven Hamiltonian, also referred to as the Floquet Hamiltonian [69–71], to extract the transition frequencies and strengths (see the inset with grey lines indicating the results from Eq. (9) of the approximate model). It can be observed that even when further increasing the modulation strength, no significant spurious transitions emerge as the strength of the parametric-activated bSWAP interaction reaches approximately 15 MHz and 10 MHz (substantially larger than those achieved in transmon-based systems [40, 45–48]) for systems with coupling strengths $J_{ck}/2\pi = 500$ MHz and $J_{ck}/2\pi = 300$ MHz, respectively. These results suggest that entangling gates based on the parametric-activated $|11\rangle \rightarrow |22\rangle$ transition can be successfully implemented with gate lengths below 100 ns, as will be illustrated in the following section.

IV. CZ GATE IMPLEMENTATIONS BASED ON THE BSWAP INTERACTION

Given the availability of strong parametric-activated bSWAP interactions in the current architecture, here we turn to employ them to implement fast entangling gates. While the following discussion focuses on the bSWAP interaction between the plasmon modes $|1\rangle \rightarrow |2\rangle$ of the two fluxonium qubits, we note that other types of activated bSWAP interactions, e.g., $|00\rangle \rightarrow |33\rangle$ and $|10\rangle \rightarrow |23\rangle$ as discussed in Sec. III B, can also be utilized for the same purpose. However, beyond the circuit Hamiltonian parameters utilized here to enhance the bSWAP-type interaction $|11\rangle \rightarrow |22\rangle$, the implementation of other such interactions requires careful optimization of circuit parameters, especially plasmon mode frequencies, to achieve large activated coupling strengths and reduced frequency collisions.

A. Gate error

As shown in Fig. 2(b), we consider two operational configurations: the dynamic flux-bias configuration and the static bias configuration. Figure 6(a) displays a typical control pulse (flat-top cosine pulses, see Appendix C for details) used to engineer the bSWAP-type interaction $|11\rangle \rightarrow |22\rangle$ for implementing CZ gates. In the dynamic flux-bias configuration, the control pulse consists of a dynamic flux bias pulse, which tunes the coupler from its idle point (i.e., $\Phi_{ext,s}/\Phi_0 = 0$) to the interaction point (i.e., $\Phi_{ext,s}/\Phi_0 = 0.35$), and a parametric drive pulse. In contrast, the static bias configuration requires only a parametric drive pulse, with the coupler remaining at its idle point (i.e., $\Phi_{ext,s}/\Phi_0 = 0.30$). Figures 6(b) and 6(c) illustrate the corresponding gate dynamics for the dynamic flux-bias configuration without and with the dynamic flux bias applied, respectively. The population distributions at the end of the gate operation are nearly identical in both cases, further confirming that the qubit states are effectively decoupled within this architecture and that non-adiabatic transitions during coupler bias ramping are negligible [19].

To characterize the intrinsic gate performance (excluding

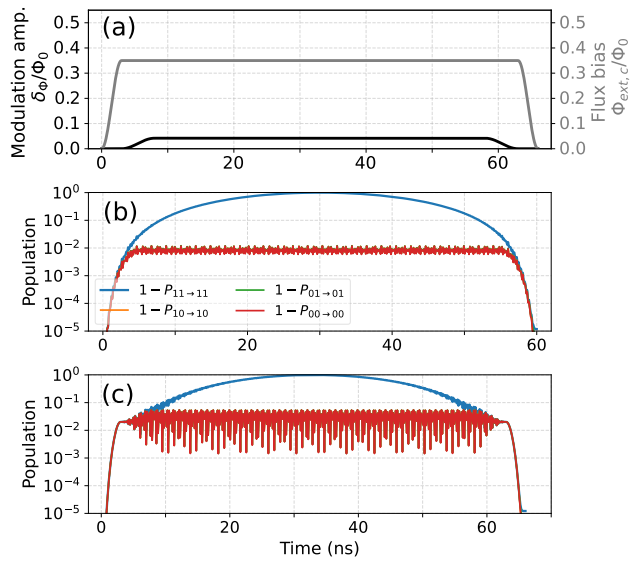


FIG. 6: (a) A typical control pulse (flat-top cosine) for implementing CZ gates in the parametric-driven fluxonium system, comprising a dynamic flux bias pulse (biasing the coupler from its idle point to the interaction point, as shown in Fig. 2) and the envelope of the parametric drive pulse. The flux pulse has a ramp time of 3 ns, and the drive pulse ramp time is 5 ns. (b) and (c) show typical system dynamics during the parametric-activated CZ gate operation without and with the dynamic flux bias, respectively. The used circuit Hamiltonian parameters are the same as those in Fig. 3(a). Here, $P_{ij \rightarrow ij}$ denotes the population remaining in state $|ij\rangle$ after initializing the system in $|ij\rangle$.

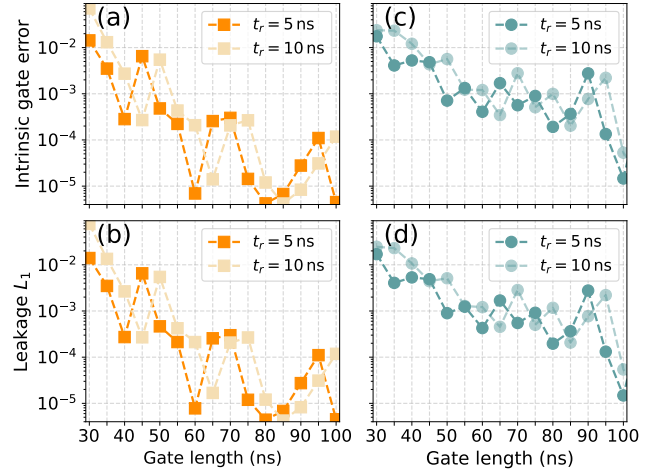


FIG. 7: (a, c) Intrinsic gate errors (excluding qubit and coupler relaxation and dephasing) and (b, d) leakage of the parametric CZ gates as functions of gate length. (a, b) and (c, d) correspond to the dynamic flux-bias configuration and the static bias configuration, respectively, see Fig. 2(b). Solid and dashed lines represent results for drive pulse ramp times of 5 ns and 10 ns, respectively.

qubit and coupler relaxation and dephasing), we consider the metric of state-average gate fidelity [72], see Appendix C for detail. For each gate length and the coupler bias setting, optimal drive parameters, including the parametric drive frequency and amplitude, can be obtained by minimizing both leakage [73] and conditional phase error [19, 74] (see Appendix C for detail). As shown in Figs. 7(a) and 7(b), the resulting gate error and leakage are shown as functions of gate length for both operational configurations. These results reveal a clear speed-fidelity trade-off: longer gate durations enable lower gate errors rates, and the gate performance is mainly limited by leakage into noncomputational states.

Besides their overall decreasing trends, both gate error and leakage also exhibit identical oscillatory behavior as a function of gate length. These features are commonly attributed to off-resonance interactions. Furthermore, varying the drive ramp times, such as increasing the ramp time from 5 ns to 10 ns, while keeping the length of the pulse flat-top constant, does not significantly alter the gate error or leakage of parametric gates with identical flat-top durations. Similar behavior is observed for both operational configurations, even though the bSWAP-type interactions are activated at markedly different drive frequencies. These results suggest that the dominant leakage mechanism may be unrelated to parametric-activated spurious transitions and is therefore independent of the drive frequency.

Moreover, as shown in Fig. 8, we assess the impact of fluxonium and coupler relaxation and dephasing on the proposed gate implementation. We assume the computational states ($|0\rangle - |1\rangle$) of the fluxonium have relaxation and dephasing times of $T_1 = 1$ ms and $T_\phi = 0.2$ ms, consistent with recent experiments (Ref. [16]). For the fluxonium plasmon transitions (e.g., $|1\rangle - |2\rangle$, $|0\rangle - |3\rangle$, $|1\rangle - |4\rangle$) and the coupler transitions, we set $T_1 = T_2$. Reflecting current technological capabilities, we further assume the fluxonium plasmon modes have a relaxation time half that of the transmon coupler. Using these parameters and solving the Lindblad master equation (see Appendix C for details) [73, 75], Figure 8 presents the total gate error, including all decoherence channels, as a function of the relaxation and dephasing times for 55-ns and 75-ns CZ gates in the two operational configurations (the drive pulse ramp time is 5 ns). For comparison, the intrinsic gate errors are also indicated for both configurations. It can be seen that, with typical coherence times on the order of $\sim 10 \mu\text{s}$ for the plasmon modes (consistent with values reported in current devices [13, 16]), fast entangling gates can achieve errors approaching 10^{-3} , which is comparable to state-of-the-art experimental demonstrations [77, 78].

To further identify the dominant error source, we also plot the errors under two simplified decoherence models: one including only relaxation and dephasing of the plasmon transition $|1\rangle - |2\rangle$ that participates in the activated bSWAP-type interaction ($|11\rangle \leftrightarrow |22\rangle$), and another including only decoherence of the computational states ($|0\rangle - |1\rangle$). As expected, for high-coherence fluxoniums, the leading gate error arises from relaxation and dephasing of the non-computational gate transition $|1\rangle \leftrightarrow |2\rangle$, consistent with earlier studies [13, 16, 19, 76].

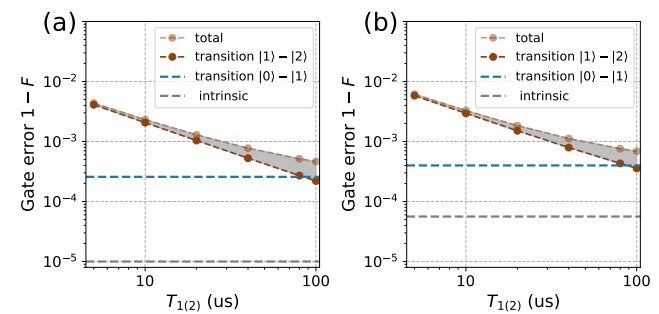


FIG. 8: Total gate error, gate error assuming only relaxation and dephasing of the plasmon transition $|1\rangle - |2\rangle$, and gate error assuming only relaxation and dephasing of qubit transition $|0\rangle - |1\rangle$ as function of the relaxation and dephasing times. For easy reference, the intrinsic gate errors are also indicated. Here, we assume $T_1 = 1$ ms and $T_\phi = 0.2$ ms for the fluxonium computational states $|0\rangle - |1\rangle$, and set $T_1 = T_2$ for fluxonium plasmon transitions ($|1\rangle - |2\rangle$, $|0\rangle - |3\rangle$, $|1\rangle - |4\rangle$) and the coupler. Additionally, the relaxation time of fluxonium plasmon modes is taken as half that of the transmon coupler. (a) and (b) correspond to the 55-ns CZ gate in dynamic flux-bias configuration and the 75-ns CZ gate in static bias configuration, respectively. Here, the drive pulse ramp time is 5 ns.

B. Leakage error analysis

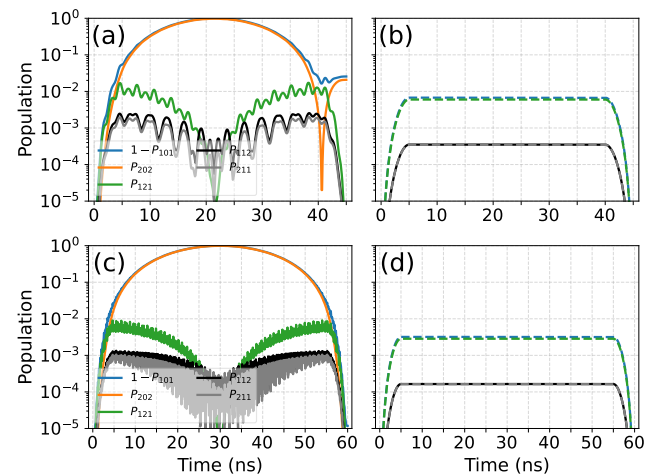


FIG. 9: Typical system dynamics of CZ gates with and without significant leakage. (a) Dynamics during a CZ gate of length 45 ns and pulse ramp time 5 ns, applied to the system initialized in $|101\rangle$. (b) Dynamics under identical parameters to (a), but with the drive frequency set to zero. (c, d) show results corresponding to (b) and (a), respectively, for a gate length of 65 ns and pulse ramp time of 5 ns.

As shown in Fig. 7, the dominant error source in current devices is expected to be relaxation and dephasing of non-computational states, based on existing demonstrated technology [13, 16]. These errors can be mitigated in future implementations through improved fabrication techniques and opti-

mization of qubit parameters and layout. However, although leakage may not represent the dominant error source in this gate architecture, it must still be carefully evaluated and minimized, particularly in the context of quantum error correction [36].

To identify the dominant leakage channel, we examine the system dynamics of CZ gates both with and without significant leakage. Figure 9(a) displays the system dynamics for a gate with substantial leakage at a gate length of 45 ns and a pulse ramp time of 5 ns. The dominant leakage channel is observed to be from $|101\rangle$ to $|121\rangle$. To verify the conjecture discussed in the previous subsection, Figure 9(b) shows the system dynamics under the same parameters as in Fig. 9(a), but with the drive frequency set to zero, i.e., effectively replacing the parametric drive with a dynamic flux pulse of identical envelope. It can be found that although no significant leakage remains at the end of the pulse, noncomputational states such as $|211\rangle$, $|211\rangle$, and $|121\rangle$ may still be temporarily populated during the flux pulse. As anticipated in Sec. II, this occurs because although the large plasmon-coupler detuning renders static bSWAP-type couplings non-dominant compared to the parametric-activated on-resonance interaction $|11\rangle \leftrightarrow |22\rangle$, these off-resonance interactions can still induce temporary populations in noncomputational states. Moreover, the parametric drive introduces additional contributions to these off-resonance interactions. Note that similar off-resonant transitions also occur in traditional transmon-based systems. However, in the present architecture, this issue is more severe because the coupled plasmon-coupler system operates in a strongly non-dispersive regime.

As shown in Fig. 9(a), off-resonant interactions generally induce time-dependent population oscillations, with periods and amplitudes determined by the specific coupling strengths g and detunings Δ , i.e., $\sim 1/\sqrt{g^2 + \Delta^2}$ and $\sim g^2/(g^2 + \Delta^2)$, respectively. Thus, during gate operations, off-resonance transitions coexist with the target transition and typically exhibit distinct oscillation periods. Consequently, even when the population oscillation from one interaction is complete, oscillations from the other interactions may remain incomplete, resulting in residual leakage as illustrated in Fig. 9(a). This leakage can be mitigated by synchronizing the population oscillations of dominant off-resonance transitions (e.g., $|101\rangle \leftrightarrow |121\rangle$) with those of the gate transition (e.g., $|101\rangle \leftrightarrow |202\rangle$) [13, 79, 80]. In the current architecture with fixed circuit parameters, such synchronization can be achieved by optimizing the flux bias or parametric drive amplitude. As demonstrated in Fig. 9(c), the synchronization of oscillations significantly reduce both leakage and intrinsic gate error, consistent with the results in Fig. 7.

Note that while synchronizing population oscillations between two transitions is generally feasible, extending this synchronization to multiple transitions presents a significant challenge. For example, as shown in Fig. 9(a), three off-resonance transitions coexist: $|101\rangle \leftrightarrow |211\rangle$, $|101\rangle \leftrightarrow |112\rangle$, and $|101\rangle \leftrightarrow |121\rangle$. In fast gates employing strong parametric drives, the strengths of these transitions can become comparable, causing the synchronization approach to fail in suppressing leakage errors to a negligible level. Since the coupler may

also be excited under these conditions, a leakage reduction operation must address both fluxonium plasmon modes and coupler excitations [81], particularly in the context of quantum error correction. This added complexity necessitates further optimization of circuit parameters, for example by increasing the anharmonicity of the transmon coupler, to effectively suppress these leakage channels.

C. Sensitivity analysis for gate parameter fluctuations

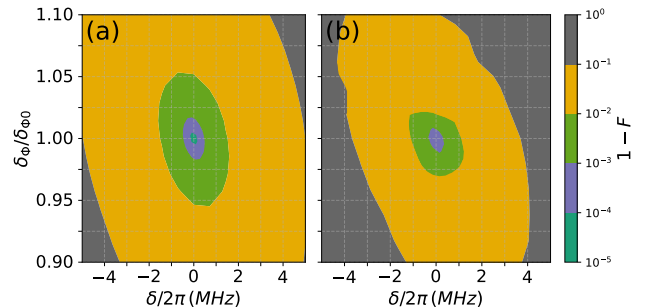


FIG. 10: Intrinsic gate error for 60-ns and 80-ns CZ gates in the two operational configurations versus drive-frequency detuning δ and normalized drive amplitude $\delta\Phi/\delta\Phi_0$ relative to their optimal values. We note that, at the optimal control points, the intrinsic errors are 6.9×10^{-6} and 1.9×10^{-4} , respectively, as shown in Figs. 7(a) and 7(c).

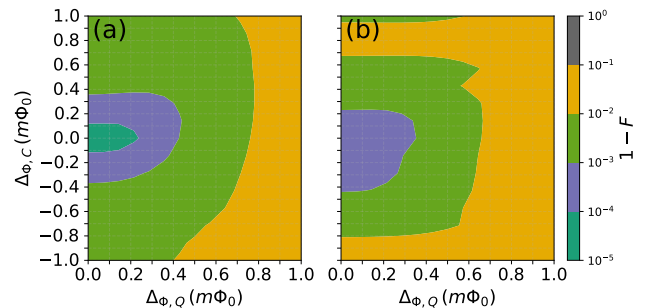


FIG. 11: Intrinsic gate error for 60-ns and 80-ns CZ gates in the two operational configurations versus qubit-bias offset $\Delta\Phi_Q$ (applied to Q_0) and coupler-bias offset $\Delta\Phi_C$ relative to their optimal values. We note that at the optimal control points, the intrinsic errors are 6.9×10^{-6} and 1.9×10^{-4} , respectively, as shown in Figs. 7(a) and 7(c).

Fluctuations or drifts in system parameters (including those of both qubits and control electronics) can degrade gate performance (see, e.g., Ref. [13, 48]). To evaluate their effect on intrinsic gate error, we analyze the sensitivity of the gate implementations to instabilities in various control parameters.

As an illustration, Figures 10 and 11 present results for 60-ns and 80-ns CZ gates in the two operational configurations

(using a 5-ns drive-pulse ramp time). Note that, at the optimal control points, the intrinsic gate errors at the optimal control points are 6.9×10^{-6} and 1.9×10^{-4} , respectively, as shown in Figs. 7(a) and 7(c). Figure 10 shows the influence of drive-parameter (frequency and amplitude) fluctuations on the gates, while Fig. 11 displays the effect of bias-parameter (flux biases on fluxonium Q_0 and the transmon coupler) fluctuations. As expected, fluctuations in system parameters do affect gate performance. At the same time, the results in these figures demonstrate that coherent gate errors below 0.001 are achievable with current experimental technology [13].

D. Spectator-induced gate error

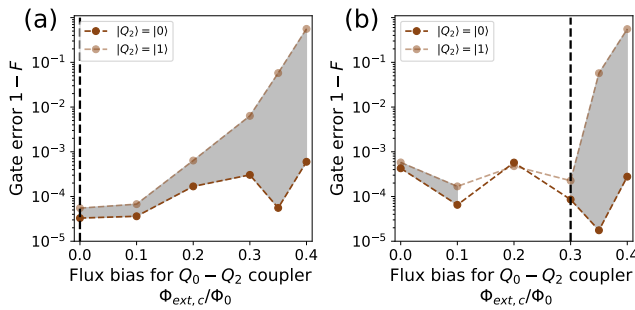


FIG. 12: Spectator-induced gate errors for the CZ gate applied to Q_0 and Q_1 as a function of the residual coupling between Q_0 and spectator fluxonium Q_2 (controlled via the bias on the $Q_0 - Q_2$ coupler; see Fig. 1(a)). Vertical dashed lines mark the bias points that suppress the residual coupling (see also in Fig. 2(a)) for suppressing the residuals. (a) 55-ns CZ gates in the dynamic flux-bias configuration with the spectator Q_2 prepared in different qubit states. (b) 75-ns CZ gates in the static flux-bias configuration with the spectator Q_2 prepared in different qubit states.

Here, to evaluate the extensibility of the proposed gate implementations, Figure 12 shows the intrinsic gate error while accounting for the residual coupling between Q_0 and spectator fluxonium Q_3 , which is controlled by the coupler flux bias for the $Q_0 - Q_2$ coupler (see Fig. 1(a)), for both operational configurations.

Following typical experimental protocols [82, 83], the CZ gate between Q_0 and Q_1 is first tuned with spectator fluxonium Q_2 in $|0\rangle$ and then characterized for both $|0\rangle$ and $|1\rangle$ states. As expected, stronger $Q_0 - Q_2$ coupling generally increases the gate error for both spectator states, with a more pronounced degradation when the spectator is in $|1\rangle$. Significantly, when the qubit-spectator coupling is suppressed, the gate fidelity approaches that of an isolated two-qubit system, and the gate performance exhibits little dependence on the spectator state. Conversely, strong coupling can lead to frequency collisions and conditional frequency shifts (see Fig. 2(a) and Ref. [19]), which substantially degrade the gate and introduce spectator-dependent correlated errors. These results, consistent with the analysis in Ref. [19], underscore

the key role of tunable plasmon interactions in mitigating spectator-induced errors.

V. CONCLUSION AND OUTLOOK

In conclusion, we propose a control strategy for fast entangling gates on scalable fluxonium architectures through parametric modulation of plasmon interaction. For the parametric-driven system, we identify and categorize three main types of parametric-activated transitions and demonstrate that, owing to the strong anharmonicity and weak qubit transition dipoles of fluxonium, bSWAP-type plasmon interactions with the strength above 10 MHz can be achieved in two typical operational configurations without being significantly affected by nearby spurious transitions. This enables the implementation of sub-100ns CZ gates with intrinsic errors below 10^{-4} in both configurations. Furthermore, this parametric modulation strategy should also be extended to implement native multi-controlled phase gates [37], further highlighting the operational flexibility in this architecture.

Similar to the microwave-based approach [12–14, 16, 19], the present technique also faces specific challenges. We show that since parametric-activated CZ gates involve temporary occupation of noncomputational states, the dominant gate error in practical devices is expected to arise from relaxation and dephasing of doubly excited plasmon states. Given current coherence times on the order of $10 \mu\text{s}$ [13, 16], achieving gate errors approaching 10^{-4} requires further improvement of plasmon coherence, which may be realized by optimizing chip fabrication, fluxonium parameters, and device layout in further implementations. Additionally, since leakage into noncomputational states, particularly those involving coupler excitation, may be unavoidable, leakage reduction operations for both fluxonium and coupler excitations will be necessary in the context of quantum error correction [36]. Moreover, as the inductive shunt in a fluxonium circuit is typically implemented using a Josephson junction array [2, 30–32], the internal degrees of freedom of this array can give rise to parasitic array modes [84], which may strongly couple to the fluxonium plasmons. Therefore, in the current fluxonium system under parametric drives, device parameters must be carefully designed to prevent the activation of unwanted interactions involving these parasitic modes. Overall, driven by the pursuit of high system-level performance for quantum error correction and considering the complex spectral characteristics of fluxonium-based architectures, these requirements call for a broader architectural perspective that balances various potential issues through careful design trade-offs to enable scalable fluxonium quantum processors.

Acknowledgments

Peng Zhao would like to thank Zhuang Ma for insightful discussions. This work is supported by the National Natural Science Foundation of China (Grants No.12204050 and No.92576110) and the Guangdong Provincial Quantum

Science Strategic Initiative (Grant No. GDZX2203001). Peng Xu is supported by the National Natural Science Foundation of China (Grants No.12105146, No.12175104, and No.92565111) and the Program of State Key Laboratory of Quantum Optics Technologies and Devices (No.KF202505).

Appendix A: Effective system Hamiltonian

Following the approach in Ref. [19], we derive the effective system Hamiltonian presented in the main text. We consider a system composed of two fluxonium qubits, Q_0 and Q_1 , coupled via a transmon-based tunable coupler. The full Hamiltonian of the system is given by:

$$H^{(1)} = \sum_{k=0,1} [4E_{C,k}\hat{n}_k^2 + \frac{E_{L,k}}{2}(\hat{\varphi}_k - \varphi_{\text{ext},k})^2 - E_{J,k} \cos \hat{\varphi}_k] + J_{c0}\hat{n}_0\hat{n}_c + J_{c1}\hat{n}_1\hat{n}_c + J_{01}\hat{n}_0\hat{n}_1 + 4E_{C,c}\hat{n}_c^2 - E_{J,c} \cos(\frac{\varphi_{\text{ext},c}}{2}) \cos \hat{\varphi}_c. \quad (\text{A1})$$

By approximating the transmon coupler as an anharmonic oscillator [1] and introducing

$$\hat{\varphi}_c = \phi_{c,\text{zpf}}(\hat{a}_c^\dagger + \hat{a}_c), \quad \hat{n}_c = in_{c,\text{zpf}}(\hat{a}_c^\dagger - \hat{a}_c) \quad (\text{A2})$$

with

$$\varphi_{c,\text{zpf}} = \frac{1}{\sqrt{2}} \left[\frac{8E_{C,c}}{E_{J,c}(\varphi_{\text{ext},c})} \right]^{\frac{1}{4}}, \quad n_{c,\text{zpf}} = \frac{1}{\sqrt{2}} \left[\frac{E_{J,c}(\varphi_{\text{ext},c})}{8E_{C,c}} \right]^{\frac{1}{4}}, \quad (\text{A3})$$

the coupler Hamiltonian can be approximated by

$$H_{\text{coupler}} = \omega_c \hat{a}_c^\dagger \hat{a}_c + \frac{\eta_c}{2} \hat{a}_c^\dagger \hat{a}_c^\dagger \hat{a}_c \hat{a}_c \hat{a}_c, \quad (\text{A4})$$

where a_c (a_c^\dagger) denotes the destroy (creation) operator, $\phi_{c,\text{zpf}}$ ($n_{c,\text{zpf}}$) represents the phase (number) zero-point fluctuation, and ω_c and η_c are the transition frequency and the anharmonicity of the coupler, respectively.

When focusing on a specific plasmon mode per fluxonium, e.g., $|j\rangle \rightarrow |l\rangle$ in Q_0 and $|r\rangle \rightarrow |t\rangle$ in Q_1 , we define the corresponding lowering and raising operators as follows:

$$\hat{p}_0 = |j\rangle\langle l|, \quad \hat{p}_0^\dagger = |l\rangle\langle j|, \quad (\text{A5})$$

$$\hat{p}_1 = |r\rangle\langle t|, \quad \hat{p}_1^\dagger = |t\rangle\langle r|,$$

for the plasmon modes of the two fluxoniums, with transition frequencies $\omega_{p,0}$ and $\omega_{p,1}$, respectively.

Accordingly, the full system Hamiltonian takes the following form after redefining $a = -ia$ ($a^\dagger = ia^\dagger$)

$$\hat{H}_p = \sum_{k=0,1} [\omega_{p,k}\hat{p}_k^\dagger \hat{p}_k + g_{p,ck}(\hat{p}_k + \hat{p}_k^\dagger)(\hat{a}_c + \hat{a}_c^\dagger)] + \omega_c \hat{a}_c^\dagger \hat{a}_c + \frac{\alpha_c}{2} \hat{a}_c^\dagger \hat{a}_c^\dagger \hat{a}_c \hat{a}_c + g_{p,01}(\hat{p}_0 + \hat{p}_0^\dagger)(\hat{p}_1 + \hat{p}_1^\dagger), \quad (\text{A6})$$

where

$$\begin{aligned} g_{p,c0} &= J_{c0}\langle j|\hat{n}_0|l\rangle\langle l|\hat{n}_c|0\rangle, \\ g_{p,c1} &= J_{c1}\langle r|\hat{n}_1|t\rangle\langle t|\hat{n}_c|0\rangle, \\ g_{p,01} &= J_{01}\langle j|\hat{n}_0|l\rangle\langle t|\hat{n}_1|r\rangle, \end{aligned} \quad (\text{A7})$$

represent the coupling strengths of the plasmon-coupler couplings and the direct plasmon-plasmon coupling. The magnitudes of the transition matrix elements for the plasmon modes and the coupler used in this work are summarized in Table III.

Considering that the coupled plasmon-transmon system operates in the dispersive regime, i.e., the interaction strength $g_{p,k}$ significantly smaller than the plasmon-coupler detuning $\Delta_{p,k} = |\omega_{p,k} - \omega_c|$, an effective Hamiltonian can be obtained by eliminating the direct plasmon-coupler interactions [50, 85], leading to (up to the second order in $g_{p,k}/\Delta_{p,k}$)

$$\begin{aligned} \hat{H}_{p,\text{eff}} = & \sum_{k=0,1} \left[(\omega_{p,k} + \frac{g_{p,k}^2}{\Delta_{p,k}}) \hat{p}_k^\dagger \hat{p}_k \right] \\ & + \left(\omega_c - \sum_{k=0,1} \frac{g_{p,k}^2}{\Delta_{p,k}} \right) \hat{a}_c^\dagger \hat{a}_c + \frac{\alpha_c}{2} \hat{a}_c^\dagger \hat{a}_c^\dagger \hat{a}_c \hat{a}_c \hat{a}_c \\ & + g_p(\hat{p}_0 + \hat{p}_0^\dagger)(\hat{p}_1 + \hat{p}_1^\dagger). \end{aligned} \quad (\text{A8})$$

Here, the final term represents the coupler-mediated plasmon-plasmon interaction, with strength

$$g_p = g_{p,01} + \frac{g_{p,0}g_{p,1}}{2} \left[\sum_{k=0,1} \left(\frac{1}{\Delta_{p,k}} - \frac{1}{S_{p,k}} \right) \right]. \quad (\text{A9})$$

and $S_{p,k} = \omega_{p,k} + \omega_c$.

Appendix B: spurious transition

As noted in the main text, the parametric-driven fluxonium system exhibits three primary classes of state transitions, (1) **bSWAP-type transitions for plasmon mode pairs**, (2) **Blue sideband transitions between the fluxonium plasmon modes and the coupler**, and (3) **Coupler state excitations due to effective two-photon (squeezing) drives**. Additionally, cross-resonance-like transitions arise due to strong state hybridization. The following discussion elaborates on the physical mechanisms underlying these transitions. For clarity, the following analysis is restricted to the dynamic flux-bias configuration.

1. The analysis of the spurious transition

Similar to Fig. 3(a), Figure 13 reveals the specific state transitions responsible for the chevron patterns observed across the 3-13 GHz frequency range. Corresponding detailed illustrations of the two main transition types, i.e., bSWAP-type plasmon transitions and blue sideband transitions, are provided for all four computational states in Fig. 14. Additionally, the physical mechanism underlying the cross-resonance-like transitions, facilitated by either bSWAP-type plasmon

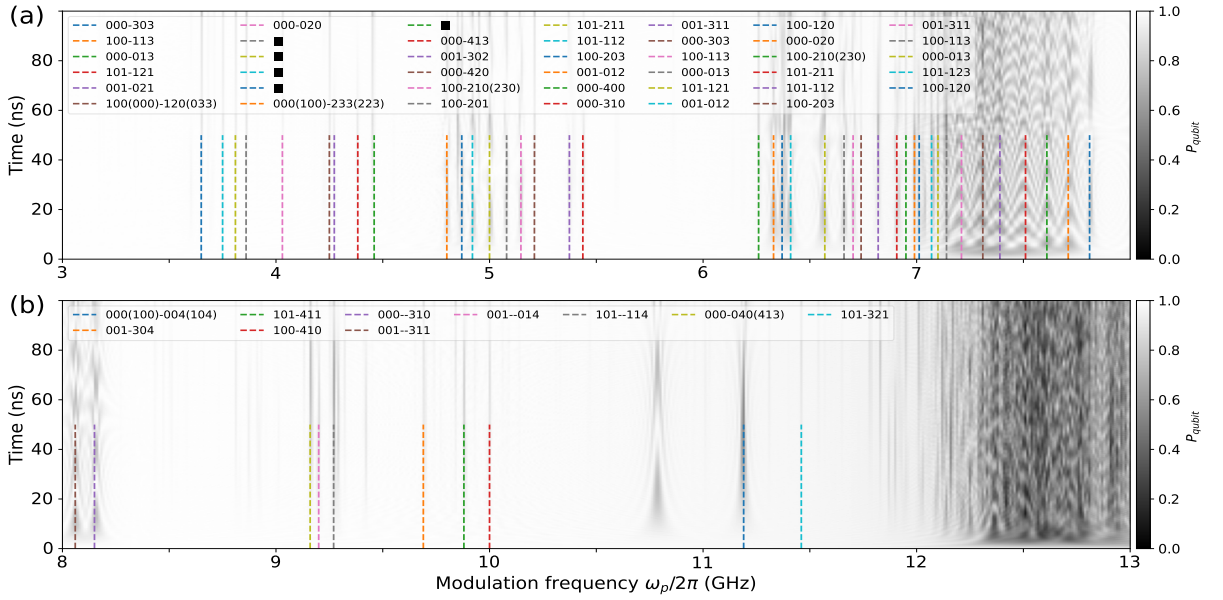


FIG. 13: Identical to Fig. 3(a), but explicitly illustrating the physical origin of the chevron patterns observed over the frequency ranges (a) 3-8 GHz and (b) 8-13 GHz. Note that the weak harmonic approximation (based on the Fock basis) for the transmon coupler may break down when describing highly excited states. Consequently, results for transitions involving such states, specifically those giving rise to the chevron pattern marked by the black square, should be considered unreliable and a more accurate description requires the use of the charge basis.

transitions or sideband transitions, is explicitly elucidated as an example.

2. Effective coupler drive

Here we provide further details regarding the effective drive experienced by the transmon coupler. As illustrated in Fig. 13, the parametric drive can induce transitions within the coupler states or transitions that involve coupler excitation, such as $|000\rangle \rightarrow |020\rangle$. To elucidate the physical mechanism underlying these transitions, we examine the case of an isolated transmon coupler subject to parametric drives.

Considering that the SQUID of the frequency-tunable transmon coupler is threaded by a time-dependent magnetic flux, the Hamiltonian of this flux-driven system takes the following form [86, 87]:

$$\hat{H}_{coupler} = 4E_{C,c}\hat{n}_c^2 + U_c, \\ U_c = -E_{J1} \cos(\hat{\varphi}_c + \alpha\varphi_{ext,c}) - E_{J2} \cos(\hat{\varphi}_c + \beta\varphi_{ext,c}) \quad (B1)$$

where E_{J1} and E_{J2} denote the Josephson energies of the two junctions in the SQUID, and α and β are parameters determined by the specific device layout [87], constrained by the relation $\alpha - \beta = 1$.

Without loss of generality, we assume $E_{J1} = E_{J2} = E_{J,c}/2$, and the external flux takes the form $\varphi_{ext,c} = \varphi_{ext,s} + \varphi_{ext,d}(t)$, where $\varphi_{ext,d} \ll 1$. The potential energy of the flux-driven transmon can then be expressed as:

$$U_c/E_{J,c} = -\cos\left(\frac{\varphi_{ext,c}}{2}\right) \cos(\hat{\varphi}_c + d\varphi_{ext,c}), \quad (B2)$$

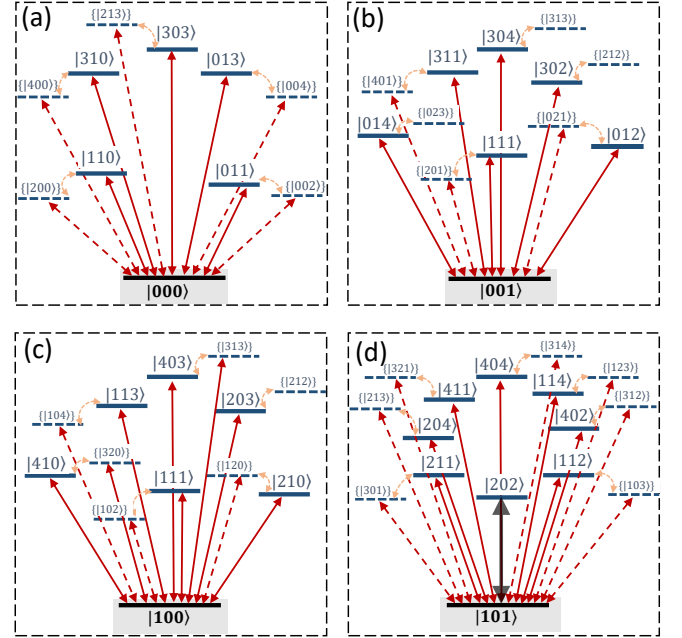


FIG. 14: A schematic illustrating parametric-activated state transitions between computational and non-computational states. (a)-(d) correspond to the computational states $|000\rangle$, $|001\rangle$, $|100\rangle$, and $|101\rangle$, respectively. In addition to the two main transition types (bSWAP-type transitions and sideband transitions, see solid red lines), cross-resonance-like spurious transitions (dashed red lines) are present, resulting from strong state hybridization induced by plasmon-coupler interactions, as indicated by the orange arrows.

where $d = \alpha + \beta$. When equal capacitance is assigned to each Josephson junction in the SQUID (i.e., $d = 0$), the potential Hamiltonian reduces to the form used in the present work, as given in Eq. (A1). In this case, expanding the potential in Eq. (B2) to second order in $\varphi_{\text{ext},d}(t)$ ($\hat{\varphi}_c$) yields the following approximate expression:

$$U_c/E_{J,c} \approx \cos\left(\frac{\varphi_{\text{ext},s}}{2}\right) \frac{\hat{\varphi}_c^2}{2} - \sin\left(\frac{\varphi_{\text{ext},s}}{2}\right) \varphi_{\text{ext},d}(t) \frac{\hat{\varphi}_c^2}{4} - \cos\left(\frac{\varphi_{\text{ext},s}}{2}\right) \varphi_{\text{ext},d}(t)^2 \frac{\hat{\varphi}_c^2}{8}. \quad (\text{B3})$$

By employing the anharmonic oscillator representation introduced in Appendix A, it can be shown that the second and third terms in Eq. (B3) correspond to an effective two-photon (squeezing) drive, i.e., $\sim (a_c a_c + a_c^\dagger a_c^\dagger)$, on the transmon coupler. This drive operates through both single- and two-photon processes. These terms can fasciate the excitation of the transmon coupler when the parametric drive frequency is resonant with state transitions involving the transmon, such as $|000\rangle \rightarrow |020\rangle$ and the transitions indicated by the black squares, which involves multiple excitations of the coupler (see Fig. 13). Note that the weak harmonic approximation (based on the Fock basis) for the transmon coupler may become invalid for highly excited states. Therefore, results for transitions involving such states, particularly those producing the chevron pattern marked by the black square, are unreliable and require a more accurate description using the charge basis.

We note that the above analysis assume a special case, where $d = 0$. i.e., in the SQUID equal capacitance is assigned to each Josephson junction. However, for actual derives, the unambiguous capacitance assignment should take into consideration of the detailed device geometric [87], which might be beyond the scope of the present work. Here we thus turn to give only the qualitative analysis for the most general case $d \neq 0$. For clarity, assuming $d\varphi_{\text{ext},c} \ll 1$ in Eq. (B2), expanding the potential in Eq. (B2) to second order in $d\varphi_{\text{ext},c}$ ($\hat{\varphi}_c$) yields the following approximate expression:

$$U_c/E_{J,c} \approx \cos\left(\frac{\varphi_{\text{ext},c}}{2}\right) \frac{\hat{\varphi}_c^2}{2} + \cos\left(\frac{\varphi_{\text{ext},c}}{2}\right) d\varphi_{\text{ext},c} \hat{\varphi}_c - \cos\left(\frac{\varphi_{\text{ext},c}}{2}\right) \frac{d^2}{6} \varphi_{\text{ext},c}^2 \hat{\varphi}_c^2. \quad (\text{B4})$$

Within the anharmonic oscillator representation framework, it can be shown that, unlike the case with $d = 0$, the general scenario $d \neq 0$ introduces not only the two-photon (squeezing) drive $\sim (a_c a_c + a_c^\dagger a_c^\dagger)$ (third term) but also a single-photon coupler drive $\sim (a_c + a_c^\dagger)$ (second term). We therefore note that under strong parametric drive, these additional coupler drive terms may induce ionization of the transmon coupler [88, 89], which could serve as another limiting factor for realizing fast, high-fidelity parametric-activated gates.

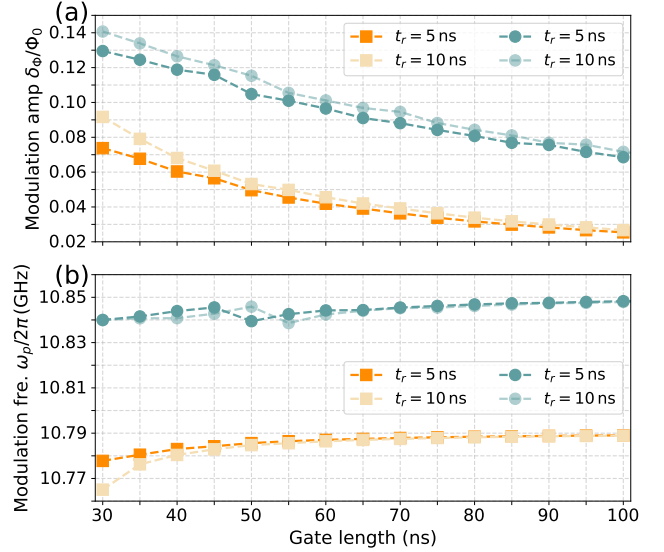


FIG. 15: The optimized gate parameters (i.e., modulation amplitudes and frequencies) used for the results shown in Figs. 6.

Appendix C: The implementation of the Parametric-activated CZ Gate

As mentioned in the main text, the CZ gate is realized by applying a parametric drive to the coupler, with the drive waveform given by:

$$\Phi(t) = \Phi_s + \Phi_d \cos(\omega_p t + \phi_0), \quad (\text{C1})$$

where Φ_s represents the static bias, Φ_d , ω_p , and ϕ_0 denotes the amplitude, frequency, and the phase of the parametric drive, respectively. For the parametric drive, we employ a flat-top cosine pulse defined by

$$\Phi_d \equiv \begin{cases} \delta_\Phi \frac{1 - \cos(\pi \frac{t}{t_r})}{2}, & 0 < t < t_r \\ \delta_\Phi, & t_r < t < t_g - t_r \\ \delta_\Phi \frac{1 - \cos(\pi \frac{t_g - t}{t_r})}{2}, & t_g - t_r < t < t_g \end{cases} \quad (\text{C2})$$

with the ramp time t_r . A similar pulse shape is also used for the dynamic flux bias in the dynamic flux-bias configuration.

Following the procedure in Refs. [37, 74], the optimized gate parameters (i.e., the drive amplitude δ_Φ and the modulation frequency ω_p , see Fig. 15) are determined by minimizing both leakage [73] and conditional phase errors within the computational subspace spanned by $\{|00\rangle, |01\rangle, |10\rangle, |11\rangle\}$. The intrinsic gate performance (excluding decoherence effects) is subsequently evaluated using the state-average gate fidelity metric [72], defined as (up to single-qubit Z rotations):

$$F = \frac{\text{Tr}(U^\dagger U) + |\text{Tr}(U_{\text{cz}}^\dagger U)|^2}{20}, \quad (\text{C3})$$

where U represents the truncated actual evolution operator within the computational subspace and U_{cz} corresponds to

the ideal CZ gate. Here the actual evolution operator U is obtained through numerical simulation of the gate dynamics, where each fluxonium is truncated to its five lowest energy levels and the transmon coupler is described in a Fock basis [1] with a dimension of 21.

We now assess the influence of fluxonium and coupler relaxation and dephasing on gate performance. Because the fidelity metric defined in Eq. (C3) is not applicable under decoherence, we adopt the average gate fidelity defined as [73, 75]

$$F = \frac{4F_p + 1 - L_1}{5}, \quad (C4)$$

where L_1 denotes the leakage of the gate operation [73] and

F_p is the process fidelity of the implemented CZ gate. Both quantities are obtained by numerically solving the Lindblad master equation [73, 75]. Note that unlike the calculation of intrinsic gate errors, the transmon coupler is here modeled as a three-level anharmonic oscillator (see Ref. [37]) to lower the computational overhead of solving the Lindblad equation, while still capturing the essential physics of the coupled fluxonium system (the same modeling approach is also used in the analysis of spectator-induced gate errors). This difference in modeling leads to distinct intrinsic gate errors for CZ gates of the same duration, i.e., the 55-ns and 75-ns CZ gates in the two operational configurations, as illustrated in Figs. 7 and 8.

[1] J. Koch, T. M. Yu, J. Gambetta, A. A. Houck, D. I. Schuster, J. Majer, A. Blais, M. H. Devoret, S. M. Girvin, and R. J. Schoelkopf, Charge-insensitive qubit design derived from the cooper pair box, *Phys. Rev. A* **76**, 042319 (2007).

[2] V. E. Manucharyan, J. Koch, L. I. Glazman, and M. H. Devoret, Fluxonium: Single Cooper-pair circuit free of charge offsets, *Science* **326**, 113 (2009).

[3] M. Brink, J. M. Chow, J. Hertzberg, E. Magesan, and Sami Rosenblatt, Device challenges for near term superconducting quantum processors: frequency collisions, *2018 IEEE Int. Electron Devices Meeting (IEDM)*, (2018).

[4] Yu Chen, C. Neill, P. Roushan, N. Leung, M. Fang, R. Barends, J. Kelly, B. Campbell, Z. Chen, B. Chiaro, A. Dunsworth, E. Jeffrey, A. Megrant, J. Y. Mutus, P. J. J. O’Malley, C. M. Quintana, D. Sank, A. Vainsencher, J. Wenner, T. C. White, Michael R. Geller, A. N. Cleland, and John M. Martinis, Qubit Architecture with High Coherence and Fast Tunable Coupling, *Phys. Rev. Lett.* **113**, 220502 (2014).

[5] J. Kelly, R. Barends, A. G. Fowler, A. Megrant, E. Jeffrey, T. C. White, D. Sank, J. Y. Mutus, B. Campbell, Yu Chen, Z. Chen, B. Chiaro, A. Dunsworth, I.-C. Hoi, C. Neill, P. J. J. O’Malley, C. Quintana, P. Roushan, A. Vainsencher, J. Wenner, A. N. Cleland, and John M. Martinis, State preservation by repetitive error detection in a superconducting quantum circuit, *Nature (London)* **519**, 66 (2015).

[6] C. Müller, J. H. Cole, and J. Lisenfeld, Towards understanding two-level-systems in amorphous solids: insights from quantum circuits, *Rep. Prog. Phys.* **82**, 124501 (2019).

[7] P. Mundada, G. Zhang, T. Hazard, and A. Houck, Suppression of Qubit Crosstalk in a Tunable Coupling Superconducting Circuit, *Phys. Rev. Appl.* **12**, 054023 (2019).

[8] R. Barends, J. Kelly, A. Megrant, A. Veitia, D. Sank, E. Jeffrey, T. C. White, J. Mutus, A. G. Fowler, B. Campbell, Y. Chen, Z. Chen, B. Chiaro, A. Dunsworth, C. Neill, P. O’Malley, P. Roushan, A. Vainsencher, J. Wenner, A. N. Korotkov, A. N. Cleland, and J. M. Martinis, Superconducting quantum circuits at the surface code threshold for fault tolerance, *Nature* **508**, 500 (2014).

[9] J. M. Kreikebaum, K. P. O’Brien, A. Morvan, and I. Siddiqi, Improving wafer-scale Josephson junction resistance variation in superconducting quantum coherent circuits, *Supercond. Sci. Technol.* **33**, 06LT02 (2020).

[10] J. B. Hertzberg, E. J. Zhang, S. Rosenblatt, E. Magesan, J. A. Smolin, J.-B. Yau, V. P. Adiga, M. Sandberg, M. Brink, J. M. Chow, and J. S. Orcutt, Laser-annealing Josephson junctions for yielding scaled-up superconducting quantum processors, *npj Quantum Inf.* **7**, 129 (2021).

[11] D. P. Pappas, M. Field, C. J. Kopas, J. A. Howard, X. Wang, E. Lachman, J. Oh, L. Zhou, A. Gold, G. M. Stiehl, K. Yadavalli, E. A. Sete, A. Bestwick, M. J. Kramer, and J. Y. Mutus, Alternating-bias assisted annealing of amorphous oxide tunnel junctions, *Commun Mater* **5**, 150 (2024).

[12] K. N. Nesterov, I. V. Pechenezhskiy, C. Wang, V. E. Manucharyan, and M. G. Vavilov, Microwave-activated controlled-z gate for fixed-frequency fluxonium qubits, *Phys. Rev. A* **98**, 030301 (2018).

[13] Q. Ficheux, L. B. Nguyen, A. Somoroff, H. Xiong, K. N. Nesterov, M. G. Vavilov, and V. E. Manucharyan, Fast logic with slow qubits: Microwave-activated controlled-z gate on low-frequency fluxoniums, *Phys. Rev. X* **11**, 021026 (2021).

[14] H. Xiong, Q. Ficheux, A. Somoroff, L. B. Nguyen, E. Dogan, D. Rosenstock, C. Wang, K. N. Nesterov, M. G. Vavilov, and V. E. Manucharyan, Arbitrary controlled-phase gate on fluxonium qubits using differential ac stark shifts, *Phys. Rev. Res.* **4**, 023040 (2022).

[15] I. A. Simakov, G. S. Mazhorin, I. N. Moskalenko, N. N. Abramov, A. A. Grigorev, D. O. Moskalev, A. A. Pishchimova, N. S. Smirnov, E. V. Zikii, I. A. Rodionov, and I. S. Besedin, Coupler Microwave-Activated Controlled-Phase Gate on Fluxonium Qubits, *PRX Quantum* **4**, 040321 (2023).

[16] L. Ding, M. Hays, Y. Sung, B. Kannan, J. An, A. Di Paolo, A. H. Karamlou, T. M. Hazard, K. Azar, D. K. Kim, B. M. Niedzielski, A. Melville, M. E. Schwartz, J. L. Yoder, T. P. Orlando, S. Gustavsson, J. A. Grover, K. Serniak, and W. D. Oliver, High-fidelity, frequency-flexible two-qubit fluxonium gates with a transmon coupler, *Phys. Rev. X* **13**, 031035 (2023).

[17] E. L. Rosenfeld, C. T. Hann, D. I. Schuster, M. H. Mamin, and A. A. Clerk, High-Fidelity Two-Qubit Gates between Fluxonium Qubits with a Resonator Coupler, *PRX Quantum* **5**, 040317 (2024).

[18] H. Xiong, J. Wang, J. Song, J. Yang, Z. Bao, Y. Li, Z.-Y. Mi, H. Zhang, H.-F. Yu, Y. Song, and L. Duan, Scalable Low-overhead Superconducting Non-local Coupler with Exponentially Enhanced Connectivity, *arXiv:2502.18902*.

[19] P. Zhao, G. Zhao, S. Li, C. Zha, and M. Gong, Scalable fluxonium qubit architecture with tunable interactions between non-computational levels, *arXiv:2504.09888*.

[20] S. Singh, E. Y. Huang, J. Hu, F. Yilmaz, M. F. S. Zwanenburg, P. Kumaravadivel, S. Wang, T. V. Stefanski, and C. K. Andersen, Fast microwave-driven two-qubit gates between fluxonium

qubits with a transmon coupler, [arXiv:2504.13718](https://arxiv.org/abs/2504.13718).

[21] G. Zhu, D. G. Ferguson, V. E. Manucharyan, and J. Koch, Circuit QED with fluxonium qubits: Theory of the dispersive regime, *Phys. Rev. B* **87**, 024510 (2013).

[22] Y.-H. Lin, L. B. Nguyen, N. Grabon, J. S. Miguel, N. Pankratova, and V. E. Manucharyan, Demonstration of Protection of a Superconducting Qubit from Energy Decay, *Phys. Rev. Lett.* **120**, 150503 (2018).

[23] L. B. Nguyen, G. Koolstra, Y. Kim, A. Morvan, T. Chistolini, S. Singh, K. N. Nesterov, C. Jünger, L. Chen, Z. Pedramrazi, B. K. Mitchell, J. M. Kreikebaum, S. Puri, D. I. Santiago, and I. Siddiqi, Blueprint for a high-performance fluxonium quantum processor, *PRX Quantum* **3**, 037001 (2022).

[24] T. V. Stefanski, F. Yilmaz, E. Y. Huang, M. F. S. Zwanenburg, S. Singh, S. Wang, L. J. Splitthoff, and C. K. Andersen, Improved fluxonium readout through dynamic flux pulsing, [arXiv:2411.13437](https://arxiv.org/abs/2411.13437).

[25] G. Bothara, S. Das, K. V. Salunkhe, M. Chand, J. Deshmukh, M. P. Patankar, and R. Vijay, High-fidelity QND readout and measurement back-action in a tantalum-based high-coherence fluxonium qubit, *APL Quantum* **2**, 026103 (2025).

[26] S. Watanabe, K. Hida, K. Matsuura, and Y. Nakamura, Nondestruction fluorescence readout and high-fidelity unconditional reset of a fluxonium qubit via dissipation engineering, *Phys. Rev. A* **112**, 012624 (2025).

[27] V. E. Manucharyan, J. Koch, M. Brink, L. I. Glazman, and M. H. Devoret, Coherent oscillations between classically separable quantum states of a superconducting loop, [arXiv:0910.3039](https://arxiv.org/abs/0910.3039).

[28] H. Zhang, S. Chakram, T. Roy, N. Earnest, Y. Lu, Z. Huang, D. K. Weiss, J. Koch, and D. I. Schuster, Universal Fast-Flux Control of a Coherent, Low-Frequency Qubit, *Phys. Rev. X* **11**, 011010 (2021).

[29] T. Wang, F. Wu, F. Wang, X. Ma, G. Zhang, J. Chen, H. Deng, R. Gao, R. Hu, L. Ma, Z. Song, T. Xia, M. Ying, H. Zhan, H.-H. Zhao, and C. Deng, Efficient Initialization of Fluxonium Qubits based on Auxiliary Energy Levels, *Phys. Rev. Lett.* **132**, 230601 (2024).

[30] L. B. Nguyen, Y.-H. Lin, A. Somoroff, R. Mencia, N. Grabon, and V. E. Manucharyan, High-coherence fluxonium qubit, *Phys. Rev. X* **9**, 041041 (2019).

[31] A. Somoroff, Q. Ficheux, R. A. Mencia, H. Xiong, R. Kuzmin, and V. E. Manucharyan, Millisecond coherence in a superconducting qubit, *Phys. Rev. Lett.* **130**, 267001 (2023).

[32] F. Wang, K. Lu, H. Zhan, L. Ma, F. Wu, H. Sun, H. Deng, Y. Bai, F. Bao, X. Chang, R. Gao, X. Gao, G. Gong, L. Hu, R. Hu, H. Ji, X. Ma, L. Mao, Z. Song, C. Tang, H. Wang, T. Wang, Z. Wang, T. Xia, H. Xu, Z. Zhan, G. Zhang, T. Zhou, M. Zhu, Q. Zhu, S. Zhu, X. Zhu, Y. Shi, H.-H. Zhao, and C. Deng, High-coherence fluxonium qubits manufactured with a wafer-scale-uniformity process, *Phys. Rev. Appl.* **23**, 044064 (2025).

[33] I. N. Moskalenko, I. S. Besedin, I. A. Simakov, and A. V. Ustinov, Tunable coupling scheme for implementing two-qubit gates on fluxonium qubits, *Appl. Phys. Lett.* **119**, 194001 (2021).

[34] I. N. Moskalenko, I. A. Simakov, N. N. Abramov, A. A. Grigorev, D. O. Moskalev, A. A. Pishchimova, N. S. Smirnov, E. V. Zikiy, I. A. Rodionov, and I. S. Besedin, High fidelity two-qubit gates on fluxoniums using a tunable coupler, *npj Quantum Inf.* **8**, 130 (2022).

[35] N. Didier, E. A. Sete, M. P. d. Silva, and C. Rigetti, Analytical modeling of parametrically modulated transmon qubits, *Phys. Rev. A* **97**, 022330 (2018).

[36] K. C. Miao, M. McEwen, J. Atalaya, D. Kafri, L. P. Pryadko, A. Bengtsson, A. Opremcak, K. J. Satzinger, Z. Chen, P. V. Klimov, *et al.*, Overcoming leakage in quantum error correction, *Nature Physics* **19**, 1780 (2023).

[37] P. Zhao, P. Xu, and Z.-Y. Xue, Scalable native multi-qubit gates for fluxonium architectures with tunable plasmon interactions, [arXiv:2507.18984](https://arxiv.org/abs/2507.18984).

[38] P. Bertet, C. J. P. M. Harmans, and J. E. Mooij, Parametric coupling for superconducting qubits, *Phys. Rev. B* **73**, 064512 (2006).

[39] A. O. Niskanen, K. Harrabi, F. Yoshihara, Y. Nakamura, S. Lloyd, and J. S. Tsai, Quantum Coherent Tunable Coupling of Superconducting Qubits, *Science* **316**, 723 (2007).

[40] M. Roth, M. Ganzhorn, N. Moll, S. Filipp, G. Salis, and S. Schmidt, Analysis of a parametrically driven exchange-type gate and a two-photon excitation gate between superconducting qubits, *Phys. Rev. A* **96**, 062323 (2017).

[41] S. Poletto, J. M. Gambetta, S. T. Merkel, J. A. Smolin, J. M. Chow, A. D. Córcoles, G. A. Keefe, M. B. Rothwell, J. R. Rozen, D. W. Abraham, C. Rigetti, and M. Steffen, Entanglement of Two Superconducting Qubits in a Waveguide Cavity via Monochromatic Two-Photon Excitation, *Phys. Rev. Lett.* **109**, 240505 (2012).

[42] E. Kapit, Universal two-qubit interactions, measurement, and cooling for quantum simulation and computing, *Phys. Rev. A* **92**, 012302 (2015).

[43] P. Zhao, X. Tan, H. Yu, S.-L. Zhu, and Y. Yu, Simultaneously exciting two atoms with photon-mediated Raman interactions, *Phys. Rev. A* **95**, 063848 (2017).

[44] K. N. Nesterov, Q. Ficheux, V. E. Manucharyan, and M. G. Vavilov, Proposal for entangling gates on fluxonium qubits via a two-photon transition, *PRX Quantum* **2**, 020345 (2021).

[45] D. C. McKay, S. Filipp, A. Mezzacapo, E. Magesan, J. M. Chow, and J. M. Gambetta, Universal Gate for Fixed-Frequency Qubits via a Tunable Bus, *Phys. Rev. Appl.* **6**, 064007 (2016).

[46] X. Y. Han, T. Q. Cai, X. G. Li, Y. K. Wu, Y. W. Ma, Y. L. Ma, J. H. Wang, H. Y. Zhang, Y. P. Song, and L. M. Duan, Error analysis in suppression of unwanted qubit interactions for a parametric gate in a tunable superconducting circuit, *Phys. Rev. A* **102**, 022619 (2020).

[47] S. Li, D. Fan, M. Gong, Y. Ye, X. Chen, Y. Wu, H. Guan, H. Deng, H. Rong, H.-L. Huang, C. Zha, K. Yan, S. Guo, H. Qian, H. Zhang, F. Chen, Q. Zhu, Y. Zhao, S. Wang, C. Ying, S. Cao, J. Yu, F. Liang, Y. Xu, J. Lin, C. Guo, L. Sun, N. Li, L. Han, C.-Z. Peng, X. Zhu, and J.-W. Pan, Realization of fast all-microwave controlled-z gates with a tunable coupler, *Chin. Phys. Lett.* **39**, 030302 (2022).

[48] M. Ganzhorn, G. Salis, D. J. Egger, A. Fuhrer, M. Mergenthaler, C. Müller, P. Müller, S. Paredes, M. Pechal, M. Werninghaus and S. Filipp, Benchmarking the noise sensitivity of different parametric two-qubit gates in a single superconducting quantum computing platform, *Phys. Rev. Res.* **2**, 033447 (2020).

[49] K. Kubo and H. Goto, Fast parametric two-qubit gate for highly detuned fixed-frequency superconducting qubits using a double-transmon coupler, *Appl. Phys. Lett.* **122**, 064001 (2023).

[50] S. Bravyi, D. P. DiVincenzo, and D. Loss, Schrieffer-Wolff transformation for quantum many-body systems, *Ann. Phys.* **326**, 2973 (2011).

[51] F. Beaudoin, M. P. da Silva, Z. Dutton, and A. Blais, First-order sidebands in circuit QED using qubit frequency modulation, *Phys. Rev. A* **86**, 022305 (2012).

[52] A. Petrescu, C. L. Calonnec, C. Leroux, A. D. Paolo, P. Mundada, S. Sussman, A. Vrajitoarea, A. A. Houck, and A. Blais, Accurate Methods for the Analysis of Strong-Drive Effects in Parametric Gates, *Phys. Rev. Appl.* **19**, 044003 (2023).

[53] P. V. Klimov, J. Kelly, Z. Chen, M. Neeley, A. Megrant, B. Burkett, R. Barends, K. Arya, B. Chiaro, Y. Chen, *et al.*, Fluctuations of Energy-Relaxation Times in Superconducting Qubits, *Phys. Rev. Lett.* **121**, 090502 (2018).

[54] Z. T. Wang, P. Zhao, Z. H. Yang, Ye Tian, H. F. Yu, and S. P. Zhao, Escaping Detrimental Interactions with Microwave-Dressed Transmon Qubits, *Chin. Phys. Lett.* **40**, 070304 (2023).

[55] R. Wang, Y. Feng, Y. Zhang, J. Ding, B. Li, F. Motzoi, Y. Gao, H. Xu, Z. Yang, W. Nuerbolati, H. Yu, W. Sun, and F. Yan, Suppressing spurious transitions using spectrally balanced pulse, [arXiv:2502.10116](https://arxiv.org/abs/2502.10116).

[56] L. Chen, K.-H. Lee, C.-H. Liu, B. Marinelli, R. K. Naik, Z. Kang, N. Goss, H. Kim, D. I. Santiago, and I. Siddiqi, Scalable and Site-Specific Frequency Tuning of Two-Level System Defects in Superconducting Qubit Arrays, [arXiv:2503.04702](https://arxiv.org/abs/2503.04702).

[57] G. S. Paraoanu, Microwave-induced coupling of superconducting qubits, *Phys. Rev. B* **74**, 140504(R) (2006).

[58] C. Rigetti and M. Devoret, Fully microwave-tunable universal gates in superconducting qubits with linear couplings and fixed transition frequencies, *Phys. Rev. B* **81**, 134507 (2010).

[59] P. C. de Groot, J. Lisenfeld, R. N. Schouten, S. Ashhab, A. Lupaşcu, C. J. P. M. Harmans, and J. E. Mooij, Selective darkening of degenerate transitions demonstrated with two superconducting quantum bits, *Nat. Phys.* **6**, 763 (2010).

[60] J. M. Chow, A. D. Córcoles, J. M. Gambetta, C. Rigetti, B. R. Johnson, J. A. Smolin, J. R. Rozen, G. A. Keefe, M. B. Rothwell, M. B. Ketchen, and M. Steffen, Simple All-Microwave Entangling Gate for Fixed-Frequency Superconducting Qubits, *Phys. Rev. Lett.* **107**, 080502 (2011).

[61] M. Malekakhlagh, E. Magesan, and D. C. McKay, First principles analysis of cross-resonance gate operation, *Phys. Rev. A* **102**, 042605 (2020).

[62] K. Heya, M. Malekakhlagh, S. Merkel, N. Kanazawa, and E. Pritchett, Floquet analysis of frequency collisions, *Phys. Rev. Appl.* **21**, 024035 (2024).

[63] P. Zhao, Mitigation of quantum crosstalk in cross-resonance-based qubit architectures, *Phys. Rev. Appl.* **20**, 054033 (2024).

[64] M. Malekakhlagh, W. Shanks, and H. Paik, Optimization of the resonator-induced PHASE gate for superconducting qubits, *Phys. Rev. A* **105**, 022607 (2022).

[65] A. Osman, J. Fernández-Pendás, C. Warren, S. Kosen, M. Scigliuzzo, A. F. Kockum, G. Tancredi, A. F. Roudsari, and J. Bylander, Mitigation of frequency collisions in superconducting quantum processors, *Phys. Rev. Res.* **5**, 043001 (2023).

[66] M. H. Goerz, F. Motzoi, K. B. Whaley, and C. P. Koch, Charting the circuit QED design landscape using optimal control theory, *npj Quantum Inf.* **3**, 37 (2017).

[67] Y. Sung, L. Ding, J. Braumüller, A. Vepsäläinen, B. Kannan, M. Kjaergaard, A. Greene, G. O. Samach, C. McNally, D. Kim, A. Melville, B. M. Niedzielski, M. E. Schwartz, J. L. Yoder, T. P. Orlando, S. Gustavsson, and W. D. Oliver, Realization of High-Fidelity CZ and ZZ-Free iSWAP Gates with a Tunable Coupler, *Phys. Rev. X* **11**, 021058 (2021).

[68] P. Zhao, D. Lan, P. Xu, G. Xue, M. Blank, X. Tan, H. Yu, and Y. Yu, Suppression of Static ZZ Interaction in an All-Transmon Quantum Processor, *Phys. Rev. Appl.* **16**, 024037 (2021).

[69] J. H. Shirley, Solution of the Schrödinger equation with a hamiltonian periodic in time, *Phys. Rev.* **138**, B979 (1965).

[70] H. Sambe, Steady states and quasienergies of a quantum mechanical system in an oscillating field, *Phys. Rev. A* **7**, 2203 (1973).

[71] J. Johansson, P. Nation, and F. Nori, QuTiP: An open-source Python framework for the dynamics of open quantum systems, *Comput. Phys. Commun.* **183**, 1760 (2012).

[72] L. H. Pedersen, N. M. Møller, and K. Mølmer, Fidelity of quantum operations, *Phys. Lett. A* **367**, 47 (2007).

[73] C. J. Wood and J. M. Gambetta, Quantification and characterization of leakage errors, *Phys. Rev. A* **97**, 032306 (2018).

[74] L. Jiang, P. Xu, S. Wu, J. A. Sun, and F. Q. Dou, Microwave-activated two-qubit gates for fixed-coupling and fixed-frequency transmon qubits, *Phys. Rev. A* **111**, 032609 (2025).

[75] P. Zhao, Y. Zhang, G. Xue, Y. Jin, and H. Yu, Tunable coupling of widely separated superconducting qubits: A possible application toward a modular quantum device, *Appl. Phys. Lett.* **121**, 032601 (2022).

[76] T. Abad, A. F. Kockum, and G. Johansson, Impact of decoherence on the delity of quantum gates leaving the computational subspace, [arXiv:2302.13885](https://arxiv.org/abs/2302.13885).

[77] H. Zhang, C. Ding, D. Weiss, Z. Huang, Y. Ma, C. Guinn, S. Sussman, S. P. Chitta, D. Chen, A. A. Houck, J. Koch, and D. I. Schuster, Tunable inductive coupler for high-fidelity gates between fluxonium qubits, *PRX Quantum* **5**, 020326 (2024).

[78] W.-J. Lin, H. Cho, Y. Chen, M. G. Vavilov, C. Wang, and V. E. Manucharyan, 24 days-stable CNOT-gate on fluxonium qubits with over 99.9% fidelity, *PRX Quantum* **6**, 010349 (2025).

[79] S. E. Economou and E. Barnes, Analytical approach to swift nonleaky entangling gates in superconducting qubits, *Phys. Rev. B* **91**, 161405(R) (2015).

[80] R. Barends, C. M. Quintana, A. G. Petukhov, Y. Chen, D. Kafri, K. Kechedzhi, R. Collins, O. Naaman, S. Boixo *et al.*, Diabatic Gates for Frequency-Tunable Superconducting Qubits, *Phys. Rev. Lett.* **123**, 210501 (2019).

[81] X. Yang, J. Chu, Z. Guo, W. Huang, Y. Liang, J. Liu, J. Qiu, X. Sun, Z. Tao, *et al.*, Coupler-Assisted Leakage Reduction for Scalable Quantum Error Correction with Superconducting Qubits, *Phys. Rev. Lett.* **133**, 170601 (2024).

[82] S. Krinner, S. Lazar, A. Remm, C.K. Andersen, N. Lacroix, G. J. Norris, C. Hellings, M. Gabureac, C. Eichler, and A. Wallraff, Benchmarking Coherent Errors in Controlled-Phase Gates due to Spectator Qubits, *Phys. Rev. Appl.* **14**, 024042 (2020).

[83] T.-Q. Cai, X.-Y. Han, Y.-K. Wu, Y.-L. Ma, J.-H. Wang, Z.-L. Wang, H.-Y. Zhang, H.-Y. Wang, Y.-P. Song, and L.-M. Duan, Impact of Spectators on a Two-Qubit Gate in a Tunable Coupling Superconducting Circuit, *Phys. Rev. Lett.* **127**, 060505 (2021).

[84] S. Sorokanich, M. Hays, and N. C. Warrington, Exact and approximate fluxonium array modes, *Phys. Rev. B* **110**, 125404 (2024).

[85] D. Zueco, G. M. Reuther, S. Kohler, and P. Hänggi, Qubit-oscillator dynamics in the dispersive regime: Analytical theory beyond the rotating-wave approximation, *Phys. Rev. A* **80**, 033846 (2009).

[86] X. You, J. A. Sauls, and J. Koch, Circuit quantization in the presence of time-dependent external flux, *Phys. Rev. B* **99**, 174512 (2019).

[87] R.-P. Riwar and D. P. DiVincenzo, Circuit quantization with time-dependent magnetic fields for realistic geometries, *npj Quantum Inf.* **8**, 36 (2022).

[88] M. Xia, C. Lledó, M. Capocci, J. Repicky, B. D’Anjou, I. Mondragon-Shem, R. Kaufman, J. Koch, A. Blais, and M. Hattridge, Exceeding the Parametric Drive Strength Threshold in Nonlinear Circuits, [arXiv:2506.03456](https://arxiv.org/abs/2506.03456).

[89] M. F. Dumas, B. Groleau-Paré, A. McDonald, M. H. M. Arias, C. Lledó, B. D’Anjou, and A. Blais, Measurement-induced transmon ionization, *Phys. Rev. X* **14**, 041023 (2025).